



Article

<https://doi.org/10.1038/s41587-023-01687-x>

Deconvolution of clinical variance in CAR-T cell pharmacology and response

Received: 14 March 2022

Accepted: 20 January 2023

Published online: 27 February 2023

Check for updates

Daniel C. Kirouac ¹, Cole Zmurchok^{1,3}, Avisek Deyati^{1,3}, Jordan Sicherman ¹, Chris Bond¹ & Peter W. Zandstra^{1,2}

Chimeric antigen receptor T cell (CAR-T) expansion and persistence vary widely among patients and predict both efficacy and toxicity. However, the mechanisms underlying clinical outcomes and patient variability are poorly defined. In this study, we developed a mathematical description of T cell responses wherein transitions among memory, effector and exhausted T cell states are coordinately regulated by tumor antigen engagement. The model is trained using clinical data from CAR-T products in different hematological malignancies and identifies cell-intrinsic differences in the turnover rate of memory cells and cytotoxic potency of effectors as the primary determinants of clinical response. Using a machine learning workflow, we demonstrate that product-intrinsic differences can accurately predict patient outcomes based on pre-infusion transcriptomes, and additional pharmacological variance arises from cellular interactions with patient tumors. We found that transcriptional signatures outperform T cell immunophenotyping as predictive of clinical response for two CD19-targeted CAR-T products in three indications, enabling a new phase of predictive CAR-T product development.

Chimeric antigen receptor T cells (CAR-Ts) have shown remarkable activity in the treatment of B cell malignancies¹. With six approved therapies and hundreds in clinical development for other hematological and solid tumors, genetically engineered T cells represent a therapeutic modality changing the drug development landscape². However, T cells bring unique challenges to therapeutic development. These so-called ‘living drugs’ proliferate, differentiate, actively traffic between tissues and engage in two-way communication with the patient immune system. The resultant pharmacology is different from that of small molecules or biologics, as there is little relationship between administered dose and exposure².

The cellular kinetics (pharmacokinetics) of circulating CAR-Ts are characterized by three distinct phases: initial expansion, followed by a rapid contraction and then slow, long-term decay³. The degree of cell expansion (Cmax) and long-term exposure (area under the curve (AUC)) vary widely among patients (approximately three orders of magnitude) and are predictive of both efficacy (tumor size reduction) and toxicity⁴. However, the product-intrinsic and host-intrinsic factors

mediating this pharmacology remain poorly defined. An empirical, non-linear mixed-effects model was developed to quantify the pharmacokinetics of Kymriah (tisagenlecleul, CTL019)⁵ and provided as part of the biologics license application (BLA)⁴. This formulation has proven applicable to multiple other CAR-T therapies in a variety of indications⁶ and has been adopted by the FDA for benchmarking^{7,8}. Although a useful tool for quantifying clinical data, the empirical equations do not account for the underlying biology and, thus, are of limited value in simulating the effects of alternate CAR-T designs, cell sources or treatment regimens. A mathematical model capable of quantitatively describing clinical data that is also based on sound biological mechanisms would be useful for the development of novel CAR-T products, as systems pharmacology modeling has proven for other therapeutic modalities⁹.

Mathematical models of T cell–tumor interactions have a long history⁷ and have been adapted to describe various aspects of CAR-T pharmacology, such as antigen binding^{8,10}, intercellular signaling¹¹, cytokine release¹², tissue distribution¹³ and competition with host T cells for

¹Notch Therapeutics, Vancouver, BC, Canada. ²School of Biomedical Engineering and Michael Smith Laboratories, University of British Columbia, Vancouver, BC, Canada. ³These authors contributed equally: Cole Zmurchok, Avisek Deyati. e-mail: dkirouac@notchtx.com

immune system reconstitution¹⁴. However, none of the above models adequately defines what limits cell expansion nor what underlies the wide variability in exposure and tumor response observed among patients¹⁵.

Insights can be gleaned by examining T cell dynamics in response to viral infection. Upon viral antigen encounter, antigen-specific T cells clonally expand and differentiate into cytotoxic effectors, which clear infected cells. After elimination of the pathogen, effector cells undergo a precipitous contraction phase, and a small percentage survive to form long-term memory T cells capable of self-renewal and recall responses. However, if the infection fails to resolve, chronic antigen stimulation leads to T cell exhaustion, wherein remnant T cells lose the ability to produce cytokines, kill target cells or proliferate in response to antigen^{16,17}. We hypothesize that an analogous process underlies the pharmacology of CAR-Ts.

We tested this hypothesis using a conceptually simple mathematical model of T cell differentiation control, wherein an antigen-driven toggle switch regulates cell fate transitions among memory, effector and exhausted T cells. We found that the model is capable of quantitatively describing CAR-T pharmacokinetic and tumor dynamic data from multiple clinical trials and deconvolutes biological mechanisms underlying clinical variance. Specifically, we identified cell-intrinsic differences in the proliferation rate of memory cells and cytotoxic potency of effectors as the primary determinants of exposure and response, and we confirmed these mathematical inferences via analysis of bulk and single-cell RNA sequencing (scRNA-seq) data. Population exposure and response predictions were validated against registrational data from Kymriah and Yescarta. Furthermore, we demonstrate that these cell-intrinsic response-mediated differences originate in the CAR-T product using a machine learning workflow that accurately predicts patient outcomes using pre-infusion product transcriptomes. We found that functional gene signatures outperform standard T cell immunophenotyping in predictive accuracy for two CD19-targeted CAR-T products in three indications, and we summarize the relative expression of these signatures across datasets via a CAR-T response scorecard. In summary, the model predicts, *de novo*, clinical variance in exposure, covariates of response and the biological mechanisms underlying the pharmacology of CAR-Ts.

Results

Model structure

We consider T cells (and CAR-T products) to comprise three functionally distinct cell populations: T memory cells (T_M), capable of long-term self-renewal and immunological memory; T effectors (T_E), responsible for target-mediated cell killing; and exhausted T cells (T_X), lacking both killing potential and proliferative capacity. An antigen-sensing toggle switch coordinately regulates the decision of memory cells to self-renew versus differentiate, the rate of effector proliferation, exhaustion and the rate of memory cell regeneration from effectors (Methods). This represents a conceptually simple yet biologically sound description of T cell function and regulatory control in response to immunological need, as determined by systemic antigen burden (Fig. 1a).

Model parameterization: patients with CLL treated with Kymriah and grouped by response

We first sought to determine whether the mathematical description of T cell regulatory control could quantitatively capture characteristic CAR-T pharmacokinetic and tumor dynamic profiles and whether parameter estimates reveal anything about biological underpinnings of clinical variability. Faietta et al.¹⁸ reported mean pharmacokinetic and tumor dynamic profiles of patients with chronic lymphocytic lymphoma (CLL) treated with Kymriah (CTL019, a CD19-targeted CAR-T), grouped by complete responders (CRs), partial responders (PRs) and non-responders (NRs). We digitized the data (mean \pm s.d.) and used particle swarm optimization (PSO) to estimate model parameters characterizing the three population archetypes (Fig. 1b). Parameters

were estimated 12 times per patient group. Although parameters are non-identifiable (Supplementary Information), the clinical data were captured with good accuracy (Supplementary Fig. 5).

Biological mechanisms differentiating CR, PR and NR populations

To decipher the biological mechanisms underlying the differing patient response profiles, parameter estimates from the three patient populations were first decomposed into principal components (PCs) (Fig. 1c). Note that the three populations form relatively distinct clusters in parameter space, wherein the x axis depicting PC1 (accounting for 35.3% of the variance) separates virtual patients by response, and the y axis depicting PC2 (accounting for 21.7% of the variance) separates CR and NR groups from PRs. Examining the coefficients of PC1 (Fig. 1d), the lowest value (associated with NR) is $TK50$ (cytotoxic potency of effectors), and the largest positive contributions (associated with CR) is memory and effector cell turnover (proliferation and death rates; μ_M , d_M and d_{E2}). That is, in responding patients, CAR-T effectors lyse target tumor cells much more efficiently, and both memory and effector cells cycle at a higher rate. These findings are consistent with local parameter sensitivity analysis (Supplementary Fig. 6).

It is established that frequency of memory cells in CAR-T infusion products, as assessed by standard T cell immunophenotyping, is predictive of clinical response^{19,20}. This was one of the primary conclusions of Faietta et al.¹⁸. However, the PC1 loadings (Fig. 1d) suggest that cell-intrinsic differences in memory cell function (μ_M and d_M) rather than frequency (f_{Tm}) are more important determinants of response. To discern the importance of memory cell frequency versus function, we performed two experiments. First, we attempted to fit the data under the hypothesis that the only difference between CR/PR/NR populations was the composition of the product (frequency of T_M , T_E and T_X cells), whereas the cell-intrinsic kinetic parameters are conserved (Supplementary Fig. 7). The model does capture differences in pharmacokinetics and tumor dynamics between the populations, and the inferred CAR-T product composition is consistent with that reported by Faietta et al.¹⁸. However, the magnitude of differences between the populations cannot be fully explained by this hypothesis. That is, CAR-T cell composition as defined by memory and exhausted cell frequencies alone is insufficient to explain the variance in clinical activity.

To directly compare the inferred differences in memory cell function among CR/PR/NR groups, we simulated a dose-ranging study using purified memory cell populations from CR/PR/NR archetypes (Supplementary Fig. 8). The CR memory cells produced robust and dose-dependent CAR-T expansion, persistence and tumor reduction, whereas the NR cells showed very little expansion or anti-tumor activity, and the PR memory cells display somewhat intermediate function. In sum, these results imply that, although memory cell frequency in CAR-T infusion products contributes to exposure and response, cell-intrinsic features, such as proliferative capacity, are necessary to account for the variance in clinical outcomes. We next sought to identify molecular signatures that underlie these cell-intrinsic features and resultant clinical variance.

Molecular and cellular features differentiating CR, PR and NR populations

To examine the molecular and cellular features underlying these functional differences, we used bulk RNA-seq data from the same trial¹⁸ wherein pre-infusion CAR-T products were sequenced and annotated by response category. Differential expression analysis on the CR versus NR populations revealed biological features (gene signatures) consistent with inferred functional differences (Supplementary Figs. 9 and 10). We confirmed findings from the original report and additionally found that the CR population is enriched in CD4⁺ and CD8⁺ memory cell gene signatures (defined by single-cell sequencing of thymic tissue²¹) and display heightened expression of signatures characterizing T cell

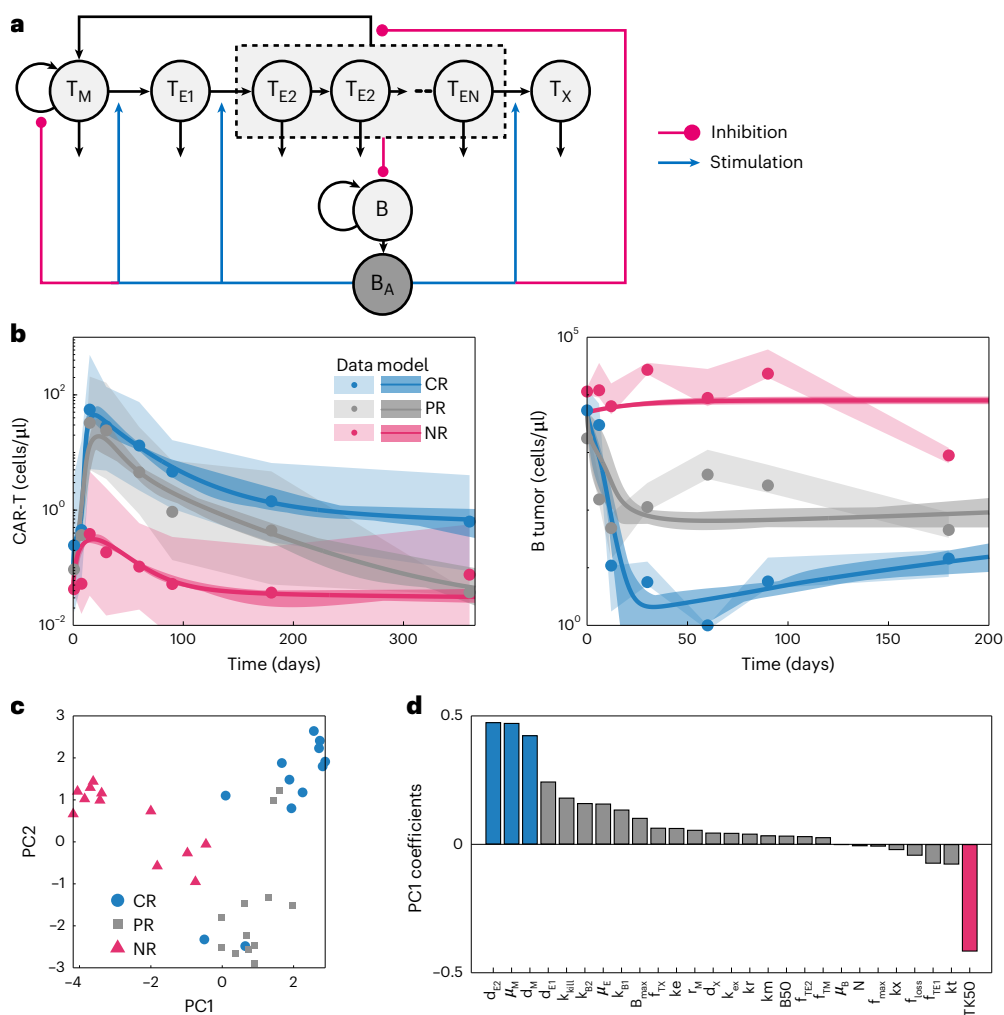


Fig. 1 | An antigen toggle switch model of T cell regulation quantitatively describes pharmacokinetics/pharmacodynamics behavior of CR, PR and NR patient population response to Kymriah in CLL. **a**, Cartoon depiction of the model structure, comprising three populations of T cells—T memory cells (T_M), T effector cells (T_{E1} and T_{E2}) and exhausted T cells (T_X)—and B cell tumors (B). Tumor cells express B cell antigen (B_A), which stimulates T cell proliferation and differentiation and inhibits the formation of T memory cells. **b**, We fit the model to published pharmacokinetics/pharmacodynamics profiles separated by response category (CR/PR/NR) from Fraietta et al.¹⁸ using PSO. Model fits

(curves: mean of 12 parameter sets; dark shaded areas: middle 90%) agree with both CAR-T and B cell tumor dynamics over time (dots: mean data; light shaded areas: range of data) for each of the three prototypic populations. **c**, PCA plot of the logarithm of the best-fitting parameters colored by population. PC1 captures 35.3% of the variability, and PC2 captures 21.7% of the variability. **d**, Sorted PC1 coefficients suggest that $TK50$ (highlighted pink bar) and k_{kill} , μ_M , and d_M (highlighted blue bars) are the largest sources of variation between CR and NR populations. These parameters correspond to cytotoxic potency, tumor cell lysis rate, memory cell proliferation and death rates, respectively.

proliferation, effector cytokine (interferon) signaling and IL2RB, IL7 and JAK/STAT signaling (defined by curated pathway databases^{22–24}). CAR-T cells from NR patients show heightened p53 (ref. ²⁵) and DNA damage²⁶ signaling pathways that may underly the proliferative deficit.

Single-sample gene set enrichment analysis (ssGSEA) was subsequently used to examine distribution of the pathway and cell signatures in individual samples. The CR population is significantly enriched in the ‘non-exhausted T cell’ signature (Fig. 2a), consistent with simulations, wherein the fraction of non-exhausted cells at day 60 (peak of anti-tumor effects) is significantly higher in the CR group (Fig. 2b), whereas cells from the NR patients rapidly progress to exhaustion (Supplementary Fig. 11). The simulations also align with clinical reports that CAR-T products that fail to expand *in vivo* show heightened expression of exhaustion markers LAG3 and PD1 (ref. ²⁷).

We found that CRs are differentially enriched in both CD8⁺ and CD4⁺ memory T cell signatures (Fig. 2c,d), consistent with the necessity of memory cells for mediating sustained responses²⁸. Note, however, that bulk sequencing data cannot resolve cell population frequencies nor

discern between transcriptionally similar versus co-varying cell types (Supplementary Fig. 12). That is, CR products may have higher frequencies of CD4⁺ and CD8⁺ memory cells or may contain cells with more ‘memory-like’ transcriptomes at similar frequencies. The CR population also shows heightened IL2RB and IL7R signaling (Fig. 2e,f), indicating that the CR cell products may show heightened sensitivity to the correspondent cytokines. Notably, IL2 and IL7 are common components of CAR-T expansion media²⁹, and peak serum IL7 concentration is predictive of CD19 CAR-T exposure and progression-free survival³⁰. Although the results shown in Fig. 2 are statistically significant, the ssGSEA distributions overlap between response categories. Thus, in addition to the limitations of bulk sequencing data, none of the gene signatures assessed could serve as univariable predictors of patient response.

Cell-intrinsic functional differences mediating CAR-T clinical response

To deconvolute the role of cell frequency versus function in mediating response, we leveraged two recently published clinical studies

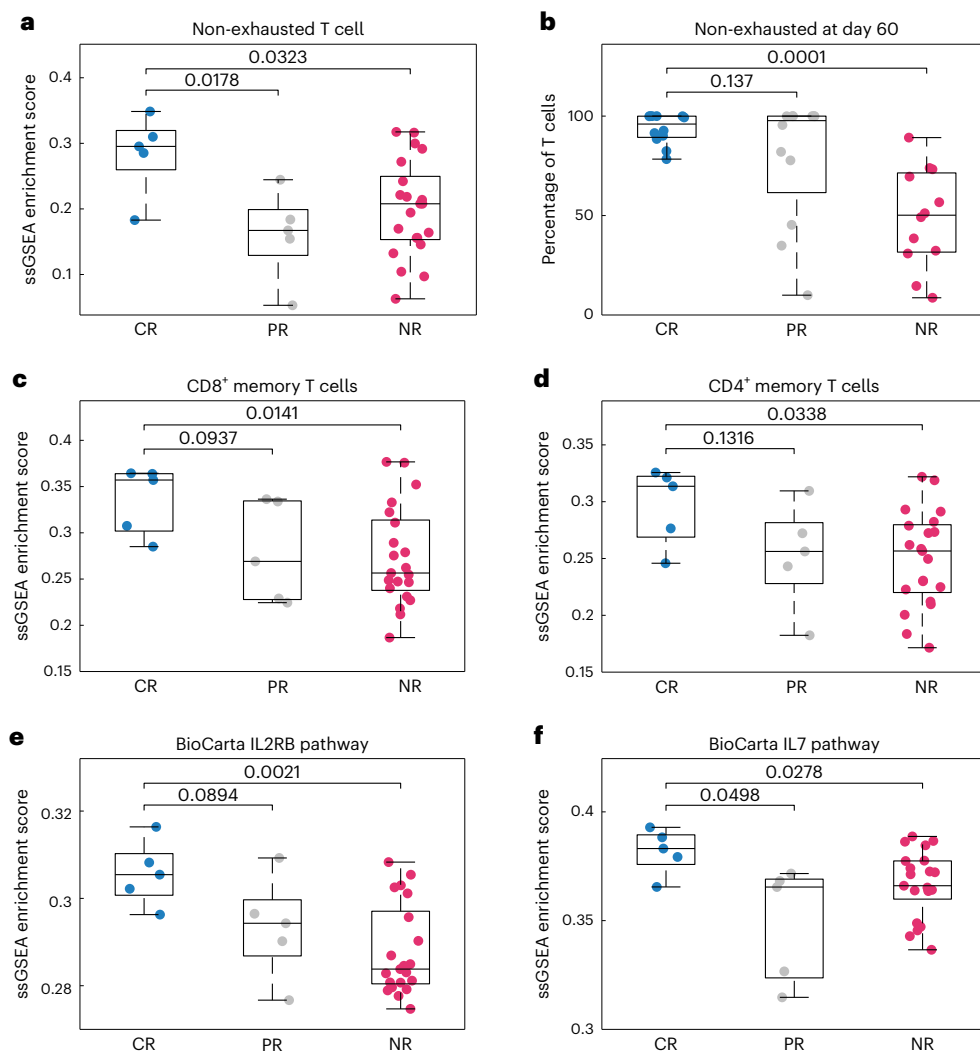


Fig. 2 | ssGSEA estimates the activity of signaling pathways and enrichment of cell populations in CAR-Ts, separated by response. a–f, ssGSEA reveals differences in cell populations and signaling pathways between populations for selected cell signatures and signaling pathways (panel titles). $n = 31$ independent samples—five CR, five PR and 21 NR. b, Using the 12 best-fitting parameter sets for each population and model simulations, we calculated the percentage of the

T cell population at day 60 that is non-exhausted. The median non-exhausted T cell population at day 60 (over the 12 parameter sets) is near 100% for both CR and PR populations, whereas the median is approximately 50% for the NR population. Differences between populations were assessed using an unequal variances two-sided *t*-test (*P* values shown). Box plots represent median \pm 25th percentiles, with whiskers representing min/max values.

containing scRNA-seq data of pre-infusion, autologous CD19 CAR-T products matched with clinical outcomes. Bai et al.³¹ reported data for 12 patients with acute lymphoblastic leukemia (ALL) treated with a CD19 CAR-T product analogous to Kymriah—five CRs, two NRs and five patients who relapsed (RL). Haradhvala et al.³² reported data for 32 patients with large B cell lymphoma (LBCL) treated with either Kymriah ($n = 13$) or Yescarta ($n = 19$). For the Kymriah-treated group, there were six CRs and seven NRs; for the Yescarta-treated group, there were 11 CRs, one PR and seven NRs.

Examination of uniform manifold approximation and projection (UMAP) projections of the three datasets (Kymriah in ALL, Kymriah in LBCL and Yescarta in LBCL) reveals some separation of response categories in transcriptome space, particularly in ALL (Fig. 3a,d,g). To assess whether response separation is attributable to differences in T cell composition, we assigned cell type labels by mapping expression profiles of the individual cells to annotated tumor-infiltrating lymphocyte populations via ProjecTILs³³. Most CD8⁺ cells in all three datasets are classified as T effector memory (Tem) or T exhausted (Tex), but there are no consistent differences in composition by response

category (Supplementary Fig. 13a–c). For example, the frequency of cells annotated as exhausted is significantly higher in the NR/RL categories as compared to CR in the ALL data ($P < 0.05$, mean 4.4% versus 8.7%, respectively; Fig. 3b,e,h). However, this pattern does not hold for the LBCL data, and the modest effect size is insufficient to account for the vast disparity in clinical outcomes. We used the cellular indexing of transcriptomes and epitopes by sequencing (CITE-seq) antibody tag data provided by Bai et al.³⁴ to assign early memory (Tmem: CD8⁺CD45RO[−]CD27⁺) and exhausted (CD8⁺PD1⁺) cell annotations by immunophenotype, reported to be predictive of response in CLL¹⁸. Although exhausted cell annotations by ProjecTILs and immunophenotype were notably concordant (6.7% versus 5.9% of total cells), cell frequencies did not differ by response category in ALL (Supplementary Fig. 13d,e).

To probe cell-intrinsic function, we annotated cells using a ‘CAR-T dysfunction’ signature, characteristic of functionally exhausted CAR-T cells with reduced proliferative and cytotoxic capacity³⁵. Visually, the dysfunction signature is dispersed throughout response categories and not restricted to exhausted regions (Fig. 3g,h,i). Interrogating

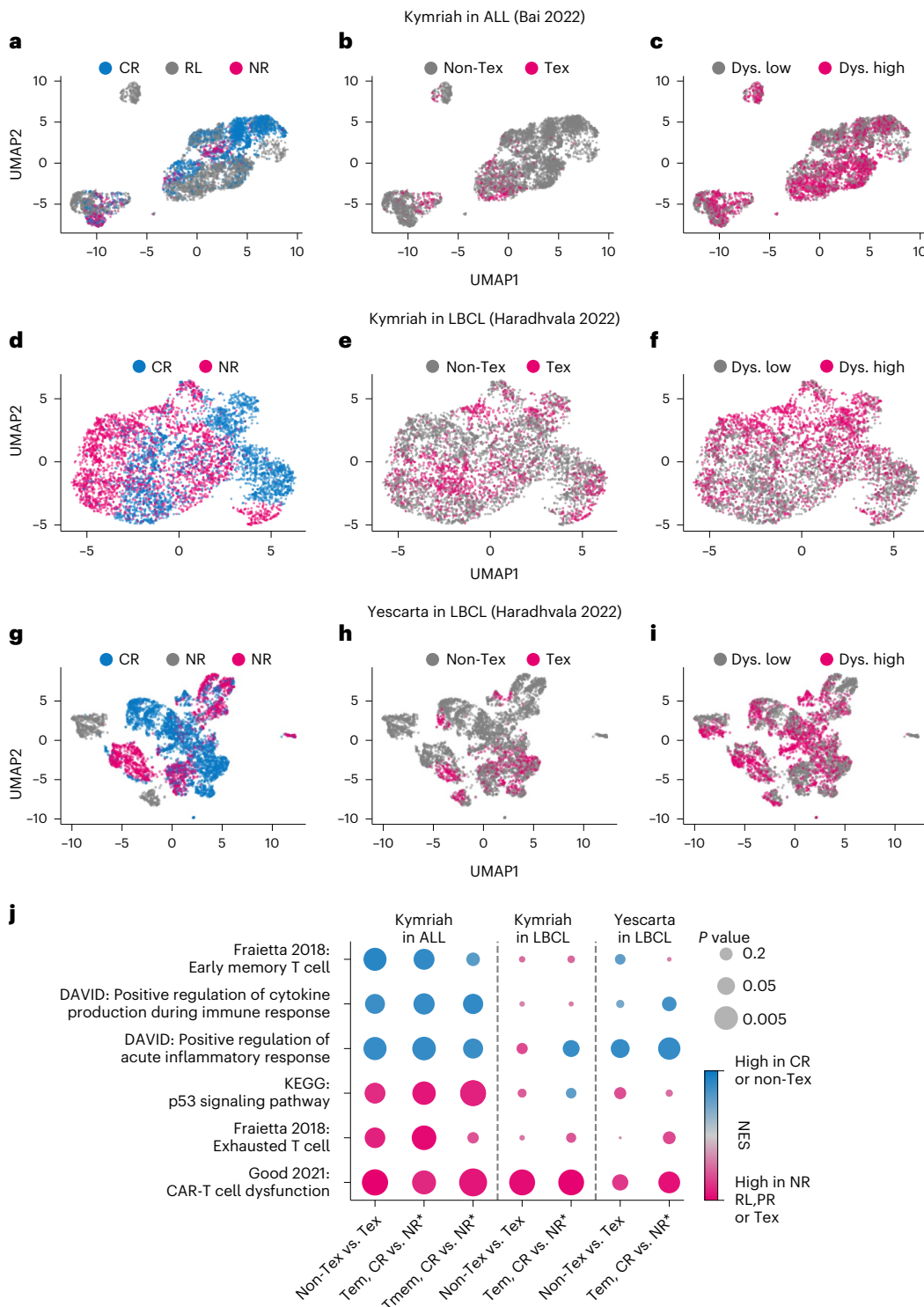


Fig. 3 | scRNA-seq of pre-infusion CAR-T products reveals cell-intrinsic defects associated with non-durable response. UMAP projections of three datasets representing Kymriah in ALL (a–c), Kymriah in LBCL (d–f) and Yescarta in LBCL (g–i). **a,d,g**, UMAP projections annotated by response category. **b,e,h**, UMAP projections annotated as exhausted using ProjectTILs³³. **c,f,i**, UMAP projections annotated for high (above mean) or low (below mean) CAR-T cell dysfunction signature from Good et al.³⁵. **j**, GSEA for select pathways, comparing

both exhausted versus non-exhausted and CR versus PR/RL/NR categories within cells annotated as T effector memory (Tem via ProjectTILs) or early memory (Tmem; CD8⁺CD45RO⁻CD27⁺ via CITE-seq). A positive normalized enrichment score (NES, blue) indicates higher enrichment in CR/non-exhausted cells. *NR = NR/RL or NR/PR. P values were calculated by Kolmogorov–Smirnov tests implemented in GSEA.

cell-intrinsic functional differences at a deeper resolution, we performed differential gene expression analysis on T sub-cell populations (annotated both by transcriptome and immunophenotype),

followed by pathway enrichment for select gene signatures (Fig. 3j). As a control, we first assessed differences between cells annotated as exhausted versus non-exhausted. Exhausted cells are consistently

enriched in the CAR-T dysfunction signature across datasets, whereas the ‘exhausted T cell’ and ‘P53 signaling’ signatures appear specific to the ALL-exhausted cells. Conversely, non-exhausted cells show disparate enrichment for the ‘early memory T cell’ signature as well as cytokine production and inflammatory response signatures, hallmarks of T cell functional potency.

Comparing cell populations from the CR versus NR/PR/RL categories reveals a consistent pattern across datasets. Focusing either on effector memory or early memory ($CD8^+CD45RA^-CD27^+$) subsets, the NR/PR/RL groups display characteristic features of exhaustion. In particular, the CAR-T dysfunction signature is consistently heightened. The CR cell populations conversely show increased expression of early memory and/or T cell functional signatures (cytokine production and inflammatory response). That is, memory and effector cell populations from CAR-T products resulting in CR appear more functional or ‘memory-like’, whereas the same cell populations from NR/PR/RL categories appear more exhausted. The single-cell data, thus, confirm inferences from the model in separate indications (ALL and LBCL): CAR-T infusion products associated with non-durable response display deficits in proliferative and functional capacity intrinsic to memory and effector cell populations.

Cell-intrinsic attributes predictive of CAR-T response can be inferred from pre-infusion product transcriptomes

If CAR-T response is product-intrinsic rather than host-intrinsic, we reasoned that the differences in pre-infusion product transcriptomes could be predictive of response. Moreover, comparing response classifiers based on cell-intrinsic function (transcriptome) versus cell composition (T cell phenotype) could help elucidate which product-intrinsic feature is more clinically relevant. We used the bulk RNA-seq data from Fraietta et al.¹⁸ to develop a multivariate transcriptome classifier. Starting with the 28 pathways that were differentially expressed between the CR versus NR groups (false discovery rate (FDR)-adjusted $P < 0.05$; Supplementary Information), we trained a logistic regression-based classifier using a genetic algorithm for feature selection (Methods).

The resultant model was able to predictively distinguish CAR-T products from CR versus NR patients, with a median cross-validated accuracy of 90% based on a train:test split of 60:40 (Fig. 4a). As comparison, we trained and assessed classifiers using the early memory ($CD8^+CD45RO^-CD27^+$) and exhausted ($CD8^+PDI^+LAG3^+$) cell frequencies as reported¹⁸ (Supplementary Fig. 13d). The resulting accuracies (80% and 83%, respectively) are significantly better than chance but less so than that achieved using functional transcriptomes ($P < 10^{-15}$ and $P = 6 \times 10^{-11}$, respectively). The gene signature panel thus reveals clinical functionality to an extent not apparent from immunotyping, implying that transcriptomes yield more value as CAR-T product characterization assays than current best-practice flow cytometry panels.

To assess whether these findings translated across datasets and indications, we applied the same workflow to pseudo-bulked single-cell data from Bai et al.³⁴ (Kymriah in ALL) and Haradhvala et al.³² (Kymriah and Yescarta in LBCL). For the Bai et al.³⁴ data (Kymriah in ALL), we compared accuracy of classifying CR versus NR/RL groups using the 28-gene signature panel to a bivariate classifier trained using the early memory ($CD8^+CD45RO^-CD27^+$) and exhausted ($CD8^+PDI^+$) immunophenotype frequencies calculated from CITE-seq antibody tags (Supplementary Fig. 13d). Median accuracy of the transcriptome classifier was 80%, less (as expected) than before but better than that achieved by T cell immunotyping (47%, $P < 10^{-15}$; Fig. 4b). We similarly assessed predictive accuracy using the LBCL data from Haradhvala et al.³² separately for Kymriah and Yescarta. As no immunophenotype data were provided, we compared the transcriptome classifier to bivariate classifiers based on estimated T effector memory (Tem) and exhausted cell (Tex) frequencies from ProjecTILs³³ annotations (Supplementary Fig. 13b,c). Median predictive accuracy of the transcriptome classifier was 80%

and 71% for Kymriah and Yescarta, respectively, outperforming T cell phenotype-based classification in both cases (60% and 67%, $P < 10^{-15}$; Fig. 4c,d). As an additional control, we seeded the classifier with ‘random’ pathways by sampling from the compendium of gene signatures that were not differentially expressed between CR versus NR groups in the CLL data (FDR-adjusted $P > 0.05$; Methods and Supplementary Fig. 14). The resulting accuracies were either slightly better or indistinguishable from chance (the ‘null’ model), and all were significantly less accurate than predictions arising from the 28-gene signature panel.

Machine learning models are notoriously difficult to interpret. To condense the inner workings of the transcriptome classifier into interpretable patterns, we created a CAR-T response scorecard (Fig. 4e). This summarizes GSEA on the 28 select pathways and frequency of inclusion in the 2,500 trained models across each of the four datasets. There is variance in the directionality and statistical significance of the signatures between datasets, as would be expected. These represent different diseases, CAR-T products and platforms, and the data were generated by independent groups. However, the overlap is far greater than would be expected by chance ($P < 10^{-5}$ for all; Methods). Notably, the Yescarta LBCL scorecard is visually distinct from the three Kymriah scorecards, and the resulting model predictions are correspondingly less accurate. This suggests distinct yet overlapping biology underlying response between the two products.

In summary, response to two separate CD19 CAR-T therapy products (Kymriah and Yescarta) in three indications (CLL, ALL and LBCL) is at least partially predetermined by functional attributes of the CAR-T infusion product. These functional attributes are shared across the four datasets to varying extents, revealed through gene signatures, and not fully apparent from T cell immunophenotyping.

Explaining inter-patient variability in Kymriah pharmacokinetics

The pharmacokinetics of Kymriah and other CAR-T products tested in clinical trials show high inter-patient variability, with AUCs spanning three orders of magnitude^{4,36,37}. Although the transcriptome classifier can predictively distinguish response categories, we assessed whether our mechanism-based model is explanatory of the additional pharmacological variability—specifically, whether a mixture of the three patient archetypes (CR/PR/NR), combined with reported variation in administered dose and initial tumor burden, is sufficient to quantitatively account for the observed variance in exposure.

We first overlaid simulations of the CR/PR/NR pharmacokinetic profiles with registrational data for Kymriah⁵. Although these are different patient populations (CLL versus B cell ALL (B-ALL)), the pharmacokinetics are highly conserved between these two indications⁶. Visually, the CR/PR/NR profiles correspond roughly to the top quartile, median and bottom 5% of exposure (Fig. 5a). Thus, the CR/PR/NR population archetypes cover much of the pharmacokinetic variation but do not fully account for individual patient variability as they were fit to population means.

We next assessed the effect of variability in dose and tumor burden using a virtual population approach⁹. We created virtual populations ($n = 1,000$) by Monte Carlo sampling across the parameter sets while randomizing dose and tumor burden within reported ranges, either alone or in combination, by log-uniform sampling.

The simulated exposures (AUC) for these virtual populations span the inter-individual variability of Kymriah (10^1 – 10^4 cells \times day / μ l; Fig. 5b). Variance in either dose or tumor burden is sufficient to cover and roughly match the reported variance of exposure within the CR/PR/NR populations. That is, although the model was fit to population mean data assuming fixed tumor burden and dose, relaxing either of these input assumptions is sufficient to account for reported variance. Similar results are produced by examining the Cmax (Fig. 5c). Grid simulations were used to assess how tumor burden and dose drive exposure and tumor response (Supplementary Fig. 15), revealing a

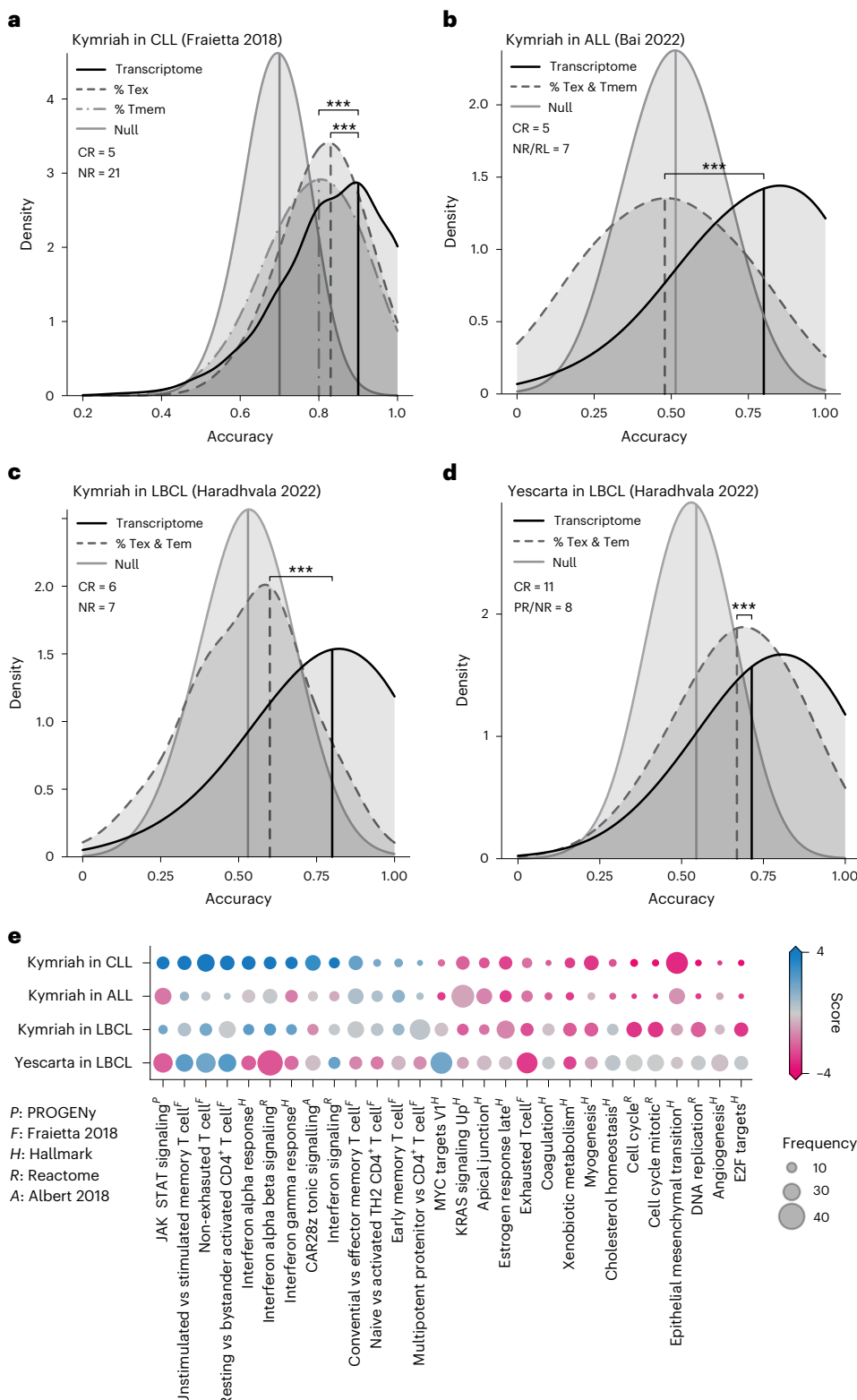


Fig. 4 | CD19 CAR-T response can be predicted from infusion products using an ssGSEA-based transcriptome classifier with better accuracy than T cell immunophenotypes. Distribution of predictive accuracies are shown for 2,500 iterations using 60:40 train:test split cross-validation. Results from the transcriptome-based ssGSEA classifier are compared to classifiers (**a**) based on reported T memory (CD8⁺CD45RO⁺CD27⁺) and T exhausted (CD8⁺PD1⁺) cell frequencies from Fraietta et al.¹⁸, **b**, A bivariate classifier based on calculated T memory (CD8⁺CD45RO⁺CD27⁺) and T exhausted (CD8⁺PD1⁺) cell frequencies from Bai et al.³⁴. **c,d**, Bivariate classifiers based on T effector memory and exhausted cell frequencies from ProjectTILs annotations of Haradhvala et al.³².

Accuracy distribution resulting from null models (random classification) is shown as controls. *** indicates $P < 10^{-15}$, two-sided rank-sum test.

e, CAR-T response scorecard, representing the 28 gene signatures fed into the transcriptome classifier, ordered by differential GSEA in Fraietta et al.¹⁸. Bubble size indicates frequency of inclusion in the 2,500 trained models after feature selection; color indicates differential enrichment between response groups by dataset, based on pseudo-bulked GSEA (score = $-1 \times \text{sign}(\text{NES}) \times \log_{10}P\text{value}$). Red, CR enriched; blue, NR/PR/RL enriched. Gene signatures are annotated by source. NES, normalized enrichment score.

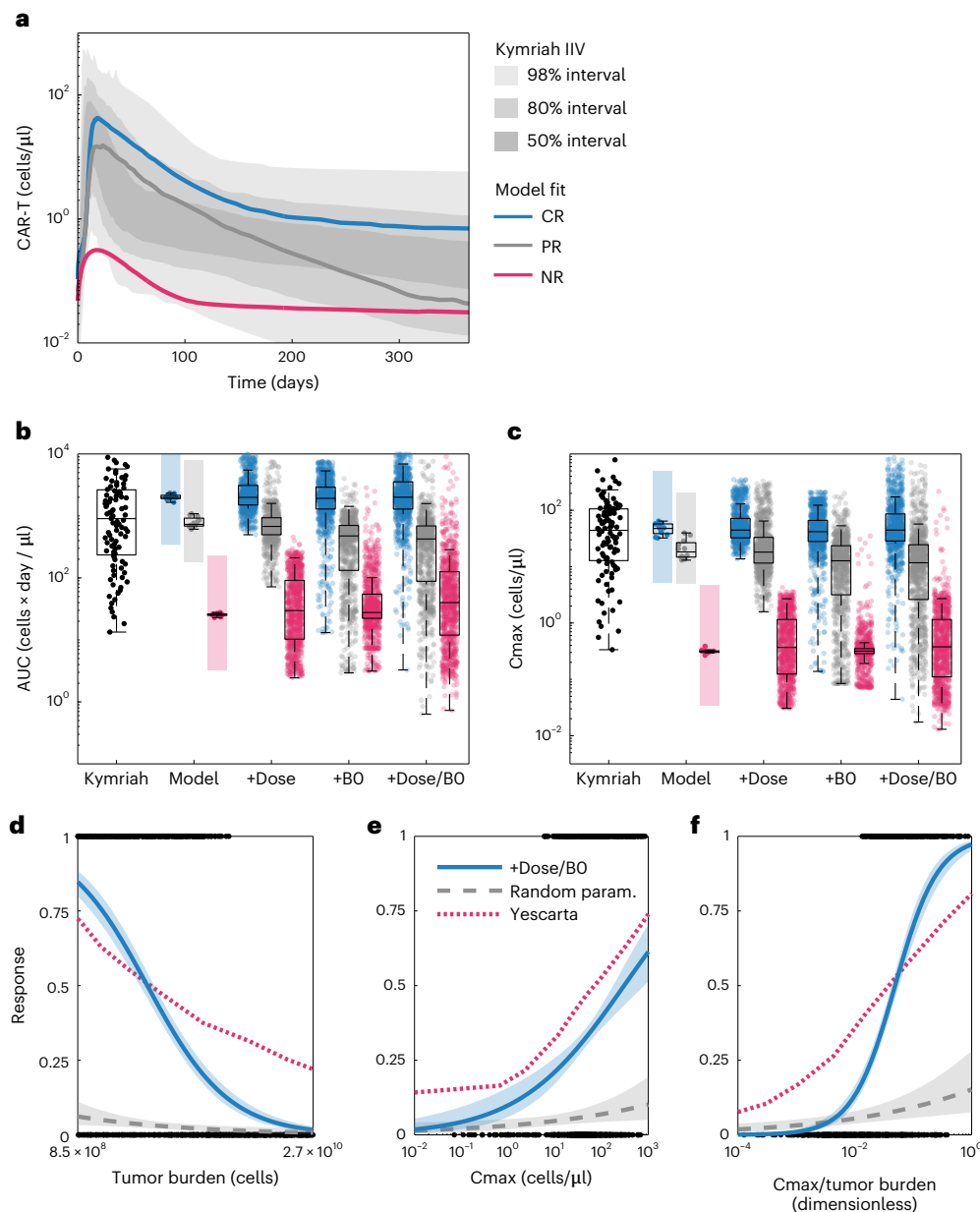


Fig. 5 | Clinical variability in dose, tumor burden and CR/PR/NR pharmacological archetype account for population variance in Kymriah exposure and predict clinical covariates of response to Yescarta. **a**, Shaded areas show the clinical variability of exposure to Kymriah⁵ with median model simulations overlaid for the CR, PR and NR populations. **b**, CAR-T AUC distributions. The box plot labeled Kymriah shows the distribution in AUC obtained from 1,000 simulations of the clinical pharmacokinetics model (each dot corresponds to a percentile of the AUC distribution). The group of box plots labeled Model shows the AUC distribution obtained for the 12 best-fitting parameter sets for each population (CR, blue; PR, gray; NR, pink) with the colored background the range of AUCs obtained from the clinical pharmacokinetics data. The group of box plots labeled +Dose shows the AUC distributions for each population when doses are randomized within reported ranges in the virtual population ($n = 1,000$); +BO shows the distributions when initial tumor burdens are randomized; and +Dose/BO shows the distribution when both dose and initial

tumor burdens are randomized. Box plots represent median \pm 25th percentiles and whiskers the min/max value or an additional 1.5-fold quartile distance. **c**, Cmax distributions plotted as in **a**. **d–f**, We defined response to treatment as tumor AUC less than 10,000 cells \times day / μ l and evaluated whether each patient in the virtual CR population with randomized doses and tumor burdens (+Dose/BO) exhibited a response (black binary data points). Logistic regression with respect to the tumor burden (**d**), Cmax (**e**) or the quotient of Cmax and tumor burden (**f**) reveals how each predicts response (blue curve indicates model estimate with 95% confidence intervals). As a control, uniform random sampling of parameter space (1,000 parameter sets) does not exhibit these response relationships (gray dashed line indicates model estimate with 95% confidence intervals). The clinical covariates of response calculated using the virtual population have the same trends as published covariates of response to Yescarta (red dotted curves). Note that the covariates of response for Yescarta have been linearly scaled to match the ranges in the virtual population for plotting.

non-linear relationship that likely contributes to the clinical variance. Given that the model recapitulates observed variance in exposure, we next assessed whether these simulations predict clinical covariates of tumor response.

Predicted covariates of response: Cmax and tumor burden
We examined whether the virtual populations could predict a priori the reported statistical relationships among cell expansion, tumor burden and clinical response. A thorough analysis of response covariates

to Yescarta in large cell B cell lymphoma (LCBCL) identified the ratio of CAR-T expansion to initial tumor burden (that is, Cmax/BO) as the strongest correlate of durable response²⁰. The same result was reported for overall survival in B-ALL³⁸, indicating that this is a conserved feature across indications. The median pharmacokinetics and population variance of Yescarta are similar to Kymriah (Supplementary Fig. 16).

Focusing on the virtual CR population, we defined response by the B cell AUC, set to 10^4 cells \times day / μl (the minimum observed for the virtual PR population). We used a logistic regression model linking response to initial tumor burden (BO), Cmax or the ratio as predictors (Fig. 5d–f). The equivalent logistic curves from Yescarta were digitized and overlaid by normalizing the x axes. The results are qualitatively consistent with the clinical data, in that these covariates are predictive of response.

To assess whether these predictions emanate directly from the model structure or necessitate model training, we created a ‘control’ virtual population by random sampling of parameter space ($n=1,000$). This control population did not reproduce the same findings, emphasizing the need for appropriate training data to make accurate predictions.

Dose–response implications: patients with multiple myeloma treated with Abecma (BCMA-CAR-T)

To better understand the relationship among dose, Cmax and tumor response, we applied the modeling framework to a phase 1/2 dose-escalation study of Abecma (BB2121, idecabtagene vicleucel), a BCMA-targeted CAR-T approved for the treatment of multiple myeloma³⁹. We again used PSO to estimate model parameters characterizing the pharmacokinetics and tumor dynamics (Fig. 6a,b). Although parameters are non-identifiable, both were captured with good accuracy (Supplementary Fig. 17), and simulations recapitulate the relationship between Cmax/Bo and tumor response identified in Fig. 5f for Kymriah and Yescarta (Supplementary Fig. 18).

The simulations yield insight into the effects of CAR-T dose on T cell population dynamics (Fig. 6c–e). The lowest dose (50 million cells) was incapable of tumor reduction and resulted in a predominance of exhausted T cells and gradual loss of memory cells. The highest dose, for which the greatest degree of tumor reduction was observed, produced the opposite response, with minimal exhaustion and a high fraction of memory cells. This is analogous to changes in T cell composition after acute versus chronic infection and provides mechanistic underpinning to the covariates identified above. That is, at an insufficient Cmax:tumor burden ratio, due either to low dose or expansion capacity, the infused CAR-T population will exhaust before clearing tumor.

To assess the predictivity of the model, we compared simulations against data from the phase 2 study, wherein patients were treated at doses of 150, 300 and 450 million cells and tumor dynamics (BCMA levels) were monitored out to 1 year (Fig. 6f,g). Although the pharmacokinetics are moderately under-predicted, the tumor dynamics are predicted with reasonable accuracy. That is, the phase 2 data (150–450 million cell doses) fall between the simulated 150 million and 450 million cell doses with similar dynamics. This is particularly notable, given that the model was trained on data going out to 2 months, whereas predictions are extrapolated out to 1 year.

Discussion

Multiple clinical studies have confirmed that robust cell expansion after CAR-T infusion is a prerequisite for clinical efficacy^{3,20,27,38,40,41}. However, inability to predictively control this pharmacology limits their clinical utility. Mechanism-based mathematical models present a path forward. When trained using appropriate datasets, such models enable the inference of underlying biological principles governing response, enable the ability to generate quantitative predictions and ultimately guide therapeutic design. We hypothesized that the

principles governing T cell dynamics during infection also govern the pharmacology of CAR-Ts, and we tested this using a mathematical model of T cell regulatory control, conceptually based on an analogy to a toggle switch. The model was trained using available clinical pharmacokinetic and tumor dynamic data, yielding biological insights and clinical predictions, some of which have been confirmed and some of which remain untested.

First, CAR-T expansion, persistence and anti-tumor response are driven by cell-intrinsic rates of turnover of memory T cell populations and cytotoxic potency of effectors. Using bulk gene expression data, we found that enrichment of memory cell signatures, heightened proliferative and inflammatory signaling and lack of exhaustion markers in pre-infusion CAR-T products correlate with response, consistent with previous work and model-predicted functional differences. Single-cell sequencing data from two additional disease indications and an additional CD19 CAR-T product confirmed that these differences between CR and NR archetypes are intrinsic to memory cell function rather than frequency in the infusion products. CAR-T products resulting in non-durable response show deficits in proliferative and functional capacity characteristic of T cell exhaustion and terminal differentiation, even within immunophenotypically indistinguishable memory and effector cell populations. These functional differences were inferred from the mathematical model and confirmed via expression of a ‘CAR-T dysfunction’ gene signature. We think that CAR-T expansion after infusion (that is, Cmax) represents an *in vivo* readout of memory T cell proliferative capacity.

We found that response categories can be accurately predicted using pre-infusion product transcriptomes in three indications (CLL, ALL and LBCL) and two CD19-targeted products (Kymriah and Yescarta). Moreover, transcriptome profiles reveal functional attributes not apparent from standard immunophenotyping, and these attributes are shared to varying extents among the datasets examined. Notably, the memory/exhaustion phenotypes identified as predictive of response in CLL did not translate to ALL, whereas the gene signature panel did. Moreover, if pre-infusion product transcriptomes are predictive of response, this implies that these pharmacological archetypes are intrinsic to the infusion product, and, thus, CAR-T efficacy could be improved through product design.

A simple, easily implemented molecular signature for efficacious (CR-like) CAR-T products would be highly valuable for guiding optimization studies. However, such a product-agnostic and indication-agnostic signature remains elusive. Our CAR-T response scorecard reveals transcriptional features that are shared to varying extents among the four datasets. Although there are statistically significant similarities, disparate molecular mechanisms appear to coordinately mediate clinical outcomes among the three datasets and particularly between the two products (Yescarta versus Kymriah). This scorecard could serve as a useful tool for CAR-T product optimization, despite some caveats that are worth noting. First, the pathways selected are derived from the first dataset examined (Kymriah in CLL). It is, thus, a visual representation of the workflow rather than a comprehensive map of features shared consistently across datasets. Second, the colors represent group-level differential pathway enrichment, whereas the classifiers were trained on ssgSEA scores. This compression loses information about the variance within sample groups, which may be important for multivariate classification. The algorithm may, thus, select signatures that do not vary significantly at the group level but nonetheless contain information (that is, large gray bubbles). Finally, many of the signatures make sense biologically (for example, JAK/STAT signaling and exhausted T cell) while others less so (for example, EMT and xenobiotic metabolism). This is an expected outcome of comparing gene lists against pathway databases—many of the signatures are manually curated with inconsistent degrees of validation, and gene lists will overlap between biological processes. We provide the underlying gene sets in the Supplementary Information.

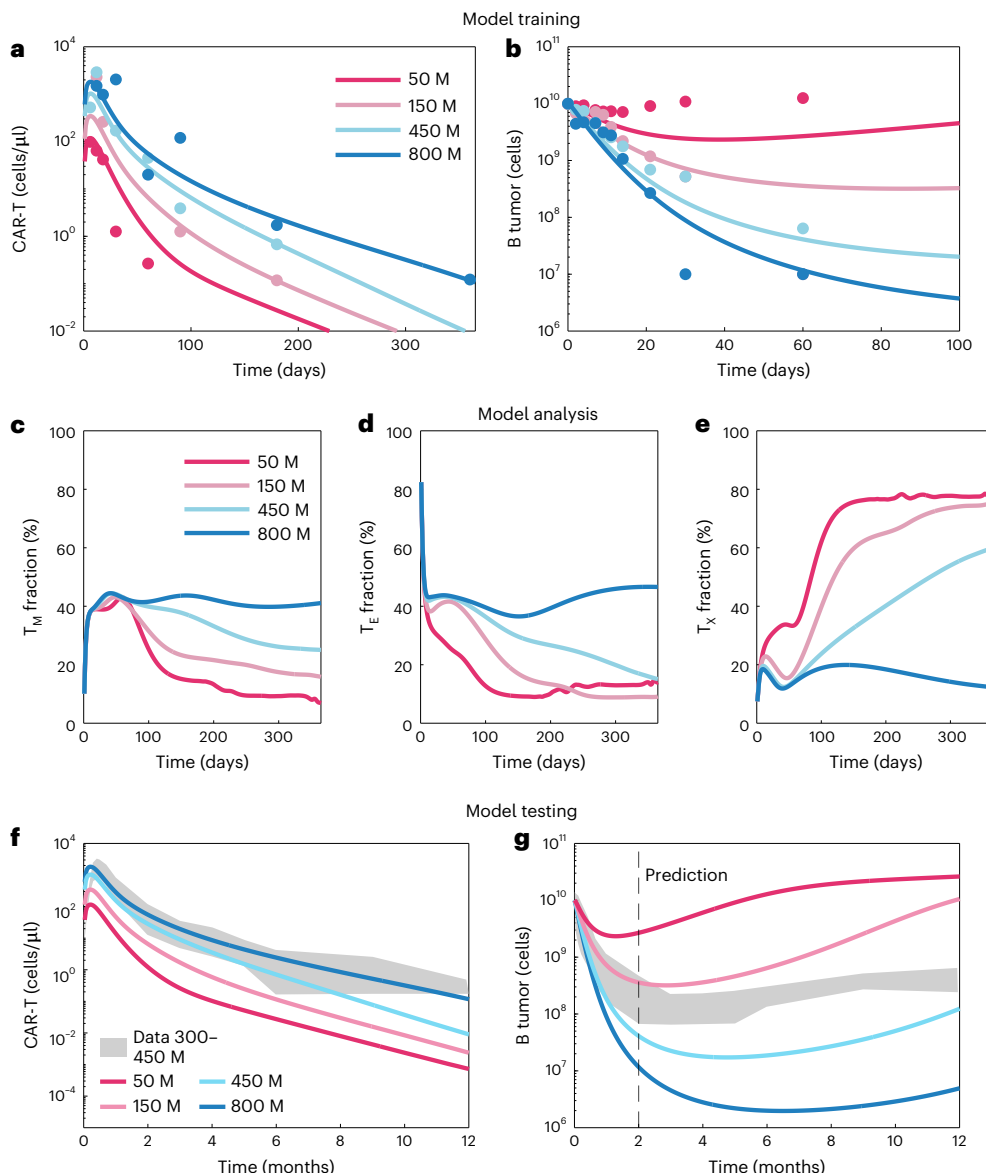


Fig. 6 | Model extension to Abecma dose response. **a,b**, Model training: we fit the toggle switch model to phase 1 dose–response data and observed good fits, with Pearson correlation coefficients from the goodness-of-fit plots (Supplementary Fig. 15) of 0.59 for the CAR-T cells and 0.74 for the tumor.

c–e, Model analysis: we compared the fraction of the total T cell population across doses in the memory, effector and exhausted groups by plotting the mean

across parameter sets. For low doses, the T cell population becomes mostly exhausted, whereas, for high doses, the population of memory and effector cells persists. **f,g**, Model testing: we compared predictive simulations at two doses with the data reported in the phase 2 study (150–450 million cell doses)⁴⁰. The tumor dynamics out to 1 year fall within the bounds predicted for the 150–450 million cell doses. M, million.

Although efforts are underway to improve CAR constructs and cell culture media, results are constrained by the autologous starting material. Cell-intrinsic differences inferred by the model and highlighted in this scorecard may emanate from the variable ‘quality’ of patient T cells at harvest⁴². If this is the case, reproducible manufacturing of highly efficacious CAR-T products will require a shift from autologous to allogeneic starting material.

We found that pharmacologic archetype, combined with variability in CAR-T cell dose and initial tumor burden, fully accounts for the inter-patient variability in exposure observed in clinical trials of Kymriah. The ratio of CAR-T expansion (C_{max}) to initial tumor burden (B_0) quantifies whether the cell product infused is capable of clearing tumor, a de novo prediction from the model observed in multiple studies of Yescarta^{20,38}. Mechanistically, we predict that cell doses insufficient to clear tumor result in exhaustion of the

CAR-Ts, whereas sufficient doses lead to regeneration of memory populations, although no longitudinal phenotyping data are available to assess this.

Controlling the clinical variability in cell dose and initial tumor burden are more immediately tractable problems than optimizing CAR-T cell design. Cell dose has historically been defined by whatever comes out of the manufacturing process, and initial tumor burden as the remnant cancer cells after lymphodepleting chemotherapy, both of which are highly variable among patients. Given consistent quality CAR-T products (for example, those displaying a CR class transcriptional signature), model simulations could be used to define patient-specific doses based on tumor burden (for example, B cell counts) to achieve an optimal balance between maximizing tumor reduction and minimizing C_{max} -associated toxicity (Supplementary Fig. 13).

Although our results suggest that the CR versus NR archetype is a product-intrinsic property, delineating product-intrinsic versus host-intrinsic sources of variability is challenging for autologous cell therapies. To start, the definitions are somewhat arbitrary and circular. For our purposes, we define product-intrinsic to mean that clinical response is predictable by properties of the infusion product. These properties (for example, memory cell proliferative capacity) may, in turn, be pre-determined by the patient's immunological state—a host-intrinsic property. Second, the definitions are blurred as many of the model parameters integrate some aspects of both. Cytotoxic potency (TK_{50}), for example, appears to be a cell-intrinsic parameter. However, this lumps together multiple cellular processes: CAR and antigen expression, CAR–antigen binding kinetics, intracellular signal transduction and engagement of cytotoxic machinery. These processes are, in turn, regulated by systemic cytokines and cell–cell interactions. A similar case could be made for most of the model parameters. Thus, although variability in CAR-T dose and tumor burden is sufficient to explain the observed variance in exposure, the inclusion of additional host-intrinsic factors may extend the model's utility. Tumor-intrinsic signaling^{43,44} and response to lymphodepletion³⁰ are two prime examples. Both have been shown to mediate CAR-T expansion and tumor response, as cytokine-mediated interactions among CAR-Ts, host T cells and tumors¹⁴ likely mediate cell-intrinsic differences.

Additional datasets would be useful to confirm these findings and extend to additional CAR-T products and disease indications. Data availability is, however, limiting. Although hundreds of CAR-T clinical studies have been conducted, raw data from most remain undisclosed, and transcriptome profiling is not routinely implemented. Access to individual patient pharmacokinetics and tumor dynamics profiles, matched with pre-infusion product transcriptomes and well-annotated clinical attributes, would be an ideal starting point to further this work and advance the science.

Online content

Any methods, additional references, Nature Portfolio reporting summaries, source data, extended data, supplementary information, acknowledgements, peer review information; details of author contributions and competing interests; and statements of data and code availability are available at <https://doi.org/10.1038/s41587-023-01687-x>.

References

- June, C. H. & Sadelain, M. Chimeric antigen receptor therapy. *N. Engl. J. Med.* **379**, 64–73 (2018).
- Awasthi, R. et al. Tisagenlecleucel cellular kinetics, dose, and immunogenicity in relation to clinical factors in relapsed/refractory DLBCL. *Blood Adv.* **4**, 560–572 (2020).
- Mueller, K. T. et al. Clinical pharmacology of tisagenlecleucel in B-cell acute lymphoblastic leukemia. *Clin. Cancer Res.* **24**, 6175–6184 (2018).
- O'Leary, M. *BLA Clinical Review Memorandum. KYMRIAH* (FDA, 2017); <https://www.fda.gov/files/vaccines%20blood%20%26%20biologics/published/Clinical-Review--KYMRIAH.pdf>
- Stein, A. M. et al. Tisagenlecleucel model-based cellular kinetic analysis of chimeric antigen receptor-T cells. *CPT Pharmacometrics Syst. Pharmacol.* **8**, 285–295 (2019).
- Liu, C. et al. Model-based cellular kinetic analysis of chimeric antigen receptor-T cells in humans. *Clin. Pharmacol. Ther.* **109**, 716–727 (2020).
- Mahlbacher, G. E., Reihmer, K. & Frieboes, H. B. Mathematical modeling of tumor-immune cell interactions. *J. Theor. Biol.* **469**, 47–60 (2019).
- Singh, A. P. et al. Bench-to-bedside translation of chimeric antigen receptor (CAR) T cells using a multiscale systems pharmacokinetic-pharmacodynamic model: a case study with anti-BCMA CAR-T. *CPT Pharmacometrics Syst. Pharmacol.* **10**, 362–376 (2021).
- Gadkar, K., Kirovac, D., Mager, D., van der Graaf, P. H. & Ramanujan, S. A six-stage workflow for robust application of systems pharmacology. *CPT Pharmacometrics Syst. Pharmacol.* **5**, 235–249 (2016).
- Singh, A. P. et al. Development of a quantitative relationship between CAR-affinity, antigen abundance, tumor cell depletion and CAR-T cell expansion using a multiscale systems PK-PD model. *MAbs* **12**, 1688616 (2019).
- Rohrs, J. A., Zheng, D., Graham, N. A., Wang, P. & Finley, S. D. Computational model of chimeric antigen receptors explains site-specific phosphorylation kinetics. *Biophys. J.* **115**, 1116–1129 (2018).
- Hardiansyah, D. & Ng, C. M. Quantitative systems pharmacology model of chimeric antigen receptor T-cell therapy. *Clin. Transl. Sci.* **12**, 343–349 (2019).
- Khot, A., Satoko, M., Thomas, V. A., Koya, R. C. & Shah, D. K. Measurement and quantitative characterization of whole-body pharmacokinetics of exogenously administered T cells in mice. *J. Pharmacol. Exp. Ther.* **368**, 503–513 (2019).
- Kimmel, G. J., Locke, F. L. & Altrock, P. M. The roles of T cell competition and stochastic extinction events in chimeric antigen receptor T cell therapy. *Proc. Biol. Sci.* **288**, 20210229 (2021).
- Chaudhury, A. et al. Chimeric antigen receptor T cell therapies: a review of cellular kinetic-pharmacodynamic modeling approaches. *J. Clin. Pharmacol.* **60**, S147–S159 (2020).
- McLane, L. M., Abdel-Hakeem, M. S. & Wherry, E. J. CD8 T cell exhaustion during chronic viral infection and cancer. *Annu. Rev. Immunol.* **37**, 1–39 (2015).
- Kaech, S. M. & Cui, W. Transcriptional control of effector and memory CD8⁺ T cell differentiation. *Nat. Rev. Immunol.* **12**, 749–761 (2012).
- Fraietta, J. A. et al. Determinants of response and resistance to CD19 chimeric antigen receptor (CAR) T cell therapy of chronic lymphocytic leukemia. *Nat. Med.* **24**, 563–571 (2018).
- Xu, Y. et al. Closely related T-memory stem cells correlate with in vivo expansion of CAR.CD19-T cells and are preserved by IL-7 and IL-15. *Blood* **123**, 3750–3759 (2014).
- Locke, F. L. et al. Tumor burden, inflammation, and product attributes determine outcomes of axicabtagene ciloleucel in large B-cell lymphoma. *Blood Adv.* **4**, 4898–4911 (2020).
- Park, J.-E. et al. A cell atlas of human thymic development defines T cell repertoire formation. *Science* **367**, eaay3224 (2020).
- Rouillard, A. D. et al. BioCarta pathways. *Harmonizome* <https://maayanlab.cloud/Harmonizome/dataset/Biocarta+Pathways> (2016).
- Liberzon, A. et al. The molecular signatures database hallmark gene set collection. *Cell Syst.* **1**, 417–425 (2015).
- Gillespie, M. et al. The reactome pathway knowledgebase 2022. *Nucleic Acids Res.* **50**, D687–D692 (2021).
- Schubert, M. et al. Perturbation-response genes reveal signaling footprints in cancer gene expression. *Nat. Commun.* **9**, 20 (2018).
- Huang, D. W., Sherman, B. T. & Lempicki, R. A. Systematic and integrative analysis of large gene lists using DAVID bioinformatics resources. *Nat. Protoc.* **4**, 44–57 (2009).
- Finney, O. C. et al. CD19 CAR T cell product and disease attributes predict leukemia remission durability. *J. Clin. Invest.* **129**, 2123–2132 (2019).
- Berger, C. et al. Adoptive transfer of effector CD8⁺ T cells derived from central memory cells establishes persistent T cell memory in primates. *J. Clin. Invest.* **118**, 294–305 (2008).
- Stock, S., Schmitt, M. & Sellner, L. Optimizing manufacturing protocols of chimeric antigen receptor T cells for improved anticancer immunotherapy. *Int. J. Mol. Sci.* **20**, 6223 (2019).

30. Hirayama, A. V. et al. The response to lymphodepletion impacts PFS in patients with aggressive non-Hodgkin lymphoma treated with CD19 CAR T cells. *Blood* **133**, 1876–1887 (2019).
31. Bai, Z. et al. Single-cell multiomics dissection of basal and antigen-specific activation states of CD19-targeted CAR T cells. *J. Immunother. Cancer* **9**, e002328 (2021).
32. Haradhvala, N. J. et al. Distinct cellular dynamics associated with response to CAR-T therapy for refractory B cell lymphoma. *Nat. Med.* **28**, 1848–1859 (2022).
33. Andreatta, M. et al. Interpretation of T cell states from single-cell transcriptomics data using reference atlases. *Nat. Commun.* **12**, 2965 (2021).
34. Bai, Z. et al. Single-cell antigen-specific landscape of CAR T infusion product identifies determinants of CD19-positive relapse in patients with ALL. *Sci. Adv.* **8**, eabj2820 (2022).
35. Good, C. R. et al. An NK-like CAR T cell transition in CAR T cell dysfunction. *Cell* **184**, 6081–6100 (2021).
36. de Claro, R. A., George, B. & McKee, A. *BLA Clinical Review Memorandum. YESCARTA* (FDA, 2017); <https://www.fda.gov/files/vaccines%20blood%20%26%20biologics/published/BLA-Clinical-Review-Memorandum--October-5--2017---YESCARTA.pdf>
37. Kaushal, M. & Natrajan, K. *BLA Clinical Review Memorandum. BREYANZI* (FDA, 2020); <https://www.fda.gov/media/146424/download>
38. Park, J. H. et al. Long-term follow-up of CD19 CAR therapy in acute lymphoblastic leukemia. *N. Engl. J. Med.* **378**, 449–459 (2018).
39. Raje, N. et al. Anti-BCMA CAR T-cell therapy bb2121 in relapsed or refractory multiple myeloma. *N. Engl. J. Med.* **380**, 1726–1737 (2019).
40. Munshi, N. C. et al. Idecabtagene vicleucel in relapsed and refractory multiple myeloma. *N. Engl. J. Med.* **384**, 705–716 (2021).
41. Porter, D. L. et al. Chimeric antigen receptor T cells persist and induce sustained remissions in relapsed refractory chronic lymphocytic leukemia. *Sci. Transl. Med.* **7**, 303ra139 (2015).
42. Shah, N. N. & Fry, T. J. Mechanisms of resistance to CAR T cell therapy. *Nat. Rev. Clin. Oncol.* **16**, 372–385 (2019).
43. Singh, N. et al. Impaired death receptor signaling in leukemia causes antigen-independent resistance by inducing CAR T-cell dysfunction. *Cancer Discov.* **10**, 552–567 (2020).
44. Scholler, N. et al. Tumor immune contexture is a determinant of anti-CD19 CAR T cell efficacy in large B cell lymphoma. *Nat. Med.* **28**, 1872–1882 (2022).

Publisher's note Springer Nature remains neutral with regard to jurisdictional claims in published maps and institutional affiliations.

Open Access This article is licensed under a Creative Commons Attribution 4.0 International License, which permits use, sharing, adaptation, distribution and reproduction in any medium or format, as long as you give appropriate credit to the original author(s) and the source, provide a link to the Creative Commons license, and indicate if changes were made. The images or other third party material in this article are included in the article's Creative Commons license, unless indicated otherwise in a credit line to the material. If material is not included in the article's Creative Commons license and your intended use is not permitted by statutory regulation or exceeds the permitted use, you will need to obtain permission directly from the copyright holder. To view a copy of this license, visit <http://creativecommons.org/licenses/by/4.0/>.

© The Author(s) 2023, corrected publication 2023

Methods

Clinical data: Kymriah

Mean pharmacokinetic and tumor dynamic profiles were digitized from a clinical study of patients with CLL treated with Kymriah, separated into CRs ($n = 8$), PRs ($n = 5$) and NRs ($n = 25$)¹⁸. Samples annotated as PR_{TD} (late relapse into B cell lymphoma) were excluded as the profiles are highly similar to the CR patients, and the biological mechanisms underlying such late relapse are unclear. Patients were treated with CAR-T doses ranging from 0.14×10^8 to 11×10^8 cells⁴¹. For parameter estimation, we assume a fixed dose of 10^8 cells, consistent with median dose used in this study and other clinical trials of Kymriah. Tumor size data were reported as B cells per microliter and were, hence, used directly in model fitting (assuming an initial tumor burden of 10^{10} total cells). Pharmacokinetics were reported as CD19 CAR transgene copies in peripheral blood (copies per microgram of genomic DNA) and were converted to cell numbers for mechanistic modeling (see below).

The non-linear mixed effects model of Kymriah cellular kinetics, as reported in the BLA⁴ and described in a subsequent publication⁵, was used to simulate population pharmacokinetics in refractory B-ALL. The model was parameterized using data compiled from two clinical studies, treated with a median dose of 10^8 cells ($n = 91$). Pharmacokinetic profiles of Kymriah in patients with CLL do not differ substantially from patients with B-ALL⁶. To compute distributions of exposure (AUC and Cmax), we simulated pharmacokinetic profiles for 1,000 virtual patients. At each timestep (0.1 days for 1 year), 1–99 percentiles were computed, and AUC and Cmax were calculated from these percentiles.

Clinical data: Abecma

Mean pharmacokinetic and tumor dynamic profiles were digitized from a phase 1 dose-escalation study of patients with refractory multiple myeloma (MM) treated with Abecma ($n = 33$), separated by dose group (50, 150, 450 and 800×10^6 cells)³⁹. Tumor size data were reported as % change in serum BCMA levels. For model fitting, we assume initial tumor burden as 10^{10} cells and linear scaling between tumor burden and reported soluble BCMA. Pharmacokinetic data were reported as transgene copies per microgram of DNA, and we applied the same scaling factor as above to convert to CAR-T cell counts. Mean pharmacokinetic and tumor dynamic profiles \pm s.d. were digitized from a phase 2 study in the same patient population ($n = 128$), treated with 150×10^8 and 450×10^6 cell doses⁴⁰ (data not separated by dose). Tumor dynamic data in this study were reported as serum BCMA (ng ml⁻¹). Data were converted to % change from baseline, again assuming initial tumor burden of 10^{10} cells for comparison to model simulations.

Scaling factors and virtual population

To estimate a scaling factor between transgene counts and cell numbers, we used data from Kalos et al.⁴⁵ wherein both counts per microgram and total circulating CD19⁺ cells were reported, estimated as $\sim 10^4$. For conversions between total cell numbers and cells per microliter for plotting, we assume a total blood volume of 2 L in humans and 2 μl in mice.

Model structure and assumptions

We encoded three functionally distinct T cell populations: T memory cells (T_M), capable of long-term regenerative capacity (self-renewal) and differentiation; T effector cells (T_E), which arise from memory population and are responsible for direct killing of tumor cells; and T exhausted cells (T_X) that lack effector function and proliferative capacity. T effectors can expand through N population doublings but lack the capacity for self-renewal. Although the mechanism remains a source of contention, T effectors can regenerate T memory cells after antigen clearance⁴⁶. The core of the mechanism-based description of T cell differentiation control is a toggle switch sensor of tumor antigen, encoded as a Hill equation (a widely used tool in pharmacological modeling⁴⁷). This toggle switch coordinately regulates rates of T memory cell self-renewal versus differentiation, proliferation and exhaustion of T effectors and regeneration of T memory cells from T effectors.

Conceptually, the idea of an antigen sensing, saturable function regulating T cell proliferation was first described by de Boer et al.⁴⁸, extended to differentiation control between memory and effector T cell fates⁴⁹ and applied to CAR-T pharmacokinetics by Martinez-Rubio et al.⁵⁰. A review of published CAR-T pharmacokinetic models in comparison to the below formulation is provided in the Supplementary Information.

We describe this control of T cell fates via a system of non-linear ordinary differential equations:

$$\begin{aligned} \frac{dT_M}{dt} &= \mu_M \cdot \left(2 \cdot f_{max} \cdot \left(1 - \frac{B_A^{km}}{B50^{km} + B_A^{km}} \right) - 1 \right) \cdot T_M + r_M \cdot \left(1 - \frac{B_A^{kr}}{B50^{kr} + B_A^{kr}} \right) \\ &\quad \cdot T_{E2} - d_M \cdot T_M, \\ \frac{dT_E}{dt} &= 2 \cdot \mu_M \cdot \left(1 - f_{max} \cdot \left(1 - \frac{B_A^{km}}{B50^{km} + B_A^{km}} \right) \right) \cdot T_M - \mu_E \cdot \left(\frac{B_A^{ke}}{B50^{ke} + B_A^{ke}} \right) \\ &\quad \cdot T_{E1} - d_E \cdot T_E \\ \frac{dT_{E2}}{dt} &= \mu_E \cdot 2^N \left(\frac{B_A^{ke}}{B50^{ke} + B_A^{ke}} \right) \cdot T_E - k_{ex} \left(\frac{B_A^{kx}}{B50^{kx} + B_A^{kx}} \right) \cdot T_{E2} - r_M \cdot \left(1 - \frac{B_A^{kr}}{B50^{kr} + B_A^{kr}} \right) \\ &\quad \cdot T_{E2} - d_{E2} \cdot T_{E2} \\ \frac{dT_X}{dt} &= k_{ex} \left(\frac{B_A^{kx}}{B50^{kx} + B_A^{kx}} \right) \cdot T_{E2} - d_X \cdot T_X \end{aligned}$$

Here, the self-renewal and differentiation of memory cells occurs at rate μ_M and is regulated through Hill equation switches that depend on the B cell antigen B_A . The parameter f_{max} describes the fraction of memory cells that self-renew versus differentiate to become effector cells. Memory cells are regenerated (with rate parameter r_M) from the T_{E2} population. We divide the effector populations into two subgroups, T_{E1} and T_{E2} , that describe the non-tumor killing and tumor killing effector populations, respectively. We made this division for mathematical simplicity: the non-tumor killing subgroup differentiates from the memory cells and forms the initial pool of effector cells that further differentiates (with rate parameter μ_E) to cytotoxic effector cells (T_{E2}). For parameter estimation routines, we encode N population doublings in a single source term in the T_{E2} equation instead of using a hierarchy of ordinary differential equations (ODEs), each tracking the number of cells that have undergone n divisions. Because we estimate N from data, it would be exceedingly complicated to dynamically update the number of ODEs in the model, as the number of population doublings changes during parameter estimation. T effector cells become exhausted with rate parameter k_{ex} , and all T cell populations are removed with corresponding rate parameters d_M , d_{E1} , d_{E2} and d_X . Note that the toggle switch, encoded as a Hill function in B cell antigen B_A , has the same half-maximum parameter $B50$ across all T cell populations but different exponents (km , kr , km , ke and kx) to account for presumed differential dose-response relationships.

We model the dynamics of B cell tumors with logistic growth with rate μ_B and carrying capacity B_{max} and non-linear tumor killing through effectors with rate k_{kill} , as well as the production and decay of B cell antigen B_A :

$$\begin{aligned} \frac{dB}{dt} &= \mu_B \cdot \left(1 - \frac{B}{B_{max}} \right) \cdot B - k_{kill} \cdot \left(\frac{T_{E2}^{kt}}{T_{E2}^{kt} + T_{E2}^{kt}} \right) \cdot B \\ \frac{dB_A}{dt} &= k_{B1} \cdot B - k_{B2} \cdot B_A \end{aligned}$$

By encoding proliferation/differentiation as driven by tumor antigen (B_A) rather than simply tumor cell number (B), the production/degradation rates (k_{B1} and k_{B2}) create a surrogate transient compartment. This allows for a time delay between changes in tumor burden and responsiveness of T cell fates. Transient compartments are commonly employed in pharmacokinetics/pharmacodynamics modeling⁵¹ to connect drug concentration to measured pharmacodynamic response.

To map cell dosing to initial condition, we implement two empirical, rapid reactions. First, a proportion of the infused cell dose is rapidly lost to account for discrepancy between cell dose and the initial conditions observed both clinically⁴⁵ and in pre-clinical models⁵¹ when cells per

microliter are reported. Second, the initial cell dose rapidly converts into the four T cell subpopulations. This reaction accounts for the fact that CAR-T products comprise mixed populations of T cells (memory, effector and exhausted states); this composition may vary and is typically not specified in clinical data. Rather than pre-specifying the composition via initial conditions, the rapid conversion reaction allows the fractions to be estimated as model parameters. This is achieved via the following set of equations where $Dose$ is the CAR-T dose administered and $DoseX$ is the remaining dose that is fractionated into the T cell subpopulations:

$$\begin{aligned}\frac{dDose}{dt} &= -(1 + f_{loss}) \cdot Dose, \\ \frac{dDoseX}{dt} &= Dose - (fraction_{TM} + fraction_{TE1} + fraction_{TE2} + fraction_{TX}) \cdot DoseX, \\ \frac{dT_M}{dt} &= fraction_{TM} \cdot DoseX, \\ \frac{dT_E1}{dt} &= fraction_{TE1} \cdot DoseX, \\ \frac{dT_E2}{dt} &= fraction_{TE2} \cdot DoseX, \\ \frac{dT_X}{dt} &= fraction_{TX} \cdot DoseX.\end{aligned}$$

We applied zero-limits to all cell populations to limit artificial regrowth. That is, if any cell population had a fractional number (<1), that cell population was set to 0. We encoded the model structure in MATLAB SimBiology (R2021a) and used PSO to estimate the model parameters based on minimization of the log mean squared error (MSE) between model simulations and data, using the ‘particleswarm’ function with 100 particles × 100 iterations and the lower limit of quantification (LLQ) set at 10^6 total cells. We fit the model separately to the CR, PR and NR populations by running the PSO algorithm 12 times for each population, generating a total of 36 parameter sets for analysis (Supplementary Table 1). Model variants based on alternate T cell population structures were also assessed for the ability to fit the data; however, none outperformed the above formulation (Supplementary Information and Supplementary Figs. 1 and 2). To assess generalizability of the model, we also fit to two pre-clinical datasets with pharmacokinetic and tumor dynamic dose–response data: CD19-CAR-T-treated NALM xenografts⁵² (Supplementary Fig. 3) and BCMA-CAR-T-treated MM1.S xenografts⁵¹ (Supplementary Fig. 4). In both cases, the model described the data with good accuracy. See Table 1 for a list of model parameters, units and lower and upper bounds used in the PSO algorithm.

Local parameter sensitivity analysis

Local parameter sensitivity coefficients (LPSCs) were computed by simulating the model and computing the CAR-T AUC and tumor AUC in response to a 10% increase in estimated parameter values across the 36 parameter sets characterizing CR/PR/NR populations. We calculated coefficients based on the median change in AUC for each population according to the formula:

$$LPSC_{Y|X} = \frac{\Delta Y/Y}{\Delta X/X} \cdot 100$$

wherein Y is the specified model output (CAR-T or tumor AUC), and X is the specified parameter.

Virtual populations

Virtual populations were created from the CR/PR/NR population fits by Monte Carlo sampling underlying parameter sets while varying CAR-T dose (10^7 – 10^9 cells) and initial tumor burden (8.5×10^8 – 2.7×10^{10} cells) within reported ranges by log-uniform sampling.

Modeling workflow

Our strategy for model-based integration of the disparate data sets was to (1) fit the pharmacokinetics/pharmacodynamics model

Table 1 | Model parameters, units and PSO bounds

Parameter	Description	Units	Lower bound	Upper bound
B50	Antigen toggle switch half-maximum	Number of antigen molecules	10^6	10^{10}
μ_B	B cell proliferation rate	1/day	0.001	0.1
k_{kill}	Rate of B cell killing by T effectors	1/day	0.001	1
f_{loss}	Fraction of dose lost	1/day	1	1000
TK50	B cell killing half-maximum	Cells	10^5	10^9
kt	B cell killing Hill exponent	Dimensionless	0.2	3
k_{B1}	Antigen generation rate	Number of antigen/(day×cell)	0.001	1
k_{B2}	Antigen clearance rate	1/day	0.001	1
μ_M	T memory proliferation rate	1/day	0.001	1
km	T memory self-renewal Hill exponent	Dimensionless	0.2	3
f_{max}	T memory maximum fraction of self-renewal	Dimensionless	0.5	0.99
ke	T effector proliferation Hill exponent	Dimensionless	0.2	3
μ_E	T effector proliferation rate	1/day	0.001	1
N	Number of population doublings in T_{E2}	Dimensionless	4	12
k_{ex}	T effector exhaustion rate	1/day	0.001	1
d_M	T memory death rate	1/day	0.001	1
d_{E1}	T effector (T_{E1}) death rate	1/day	0.001	1
d_{E2}	T effector (T_{E2}) death rate	1/day	0.001	1
d_X	T exhausted death rate	1/day	0.001	1
B_{max}	B cell tumor carrying capacity	Cells	10^8	10^{12}
k_x	T exhaustion Hill exponent	Dimensionless	0.2	3
kr	T memory regeneration Hill exponent	Dimensionless	0.2	3
r_M	T memory regeneration from T effectors	1/day	0.001	1
$fraction_{TM}$	T memory fraction of dose	1/day	1	10
$fraction_{TE1}$	T effector (T_{E1}) fraction of dose	1/day	1	10
$fraction_{TE2}$	T effector (T_{E2}) fraction of dose	1/day	30	70
$fraction_{TX}$	T exhausted fraction of dose	1/day	5	30

independently to the Fraietta et al.¹⁸ CR, PR and NR profiles; (2) create virtual populations from this model and compare the predicted population pharmacokinetic variance against Kymriah data from Stein et al.⁵ and covariates of response against Yescarta data from Locke et al.²⁰; and (3) fit the pharmacokinetics/pharmacodynamics model to Abecma dose–response data from Raje et al.³⁹ to understand mechanisms underlying the response covariates.

RNA-seq analysis

Analysis of bulk RNA-seq data was implemented within R version 4.1.1. In brief, read count data were downloaded from the supplement provided by Fraietta et al.¹⁸. Trimmed mean of M-values (TMM) normalization was implemented with edgeR (3.34.1), and normalized data were converted to log(counts per million) by applying Voom transformation.

Differential gene expression analysis was implemented with limma (3.50.3)⁵³ and gene signature analysis with ssGSEA⁵⁴. Normalized ssGSEA scores were calculated as:

$$Nij = \frac{Aij - \text{MIN}(A)}{\text{MAX}(A) - \text{MIN}(A)}$$

wherein A is the matrix of ssGSEA signature scores (i) \times samples (j). Gene signatures for cell signaling pathways were compiled from PROGENY²⁵ (10), BioCarta²² (217), Reactome²⁴ (674), Hallmark²³ (50) and DAVID²⁶ (6,577). Cell population signatures were derived from those published in Fraietta et al.¹⁸ (7), a single-cell atlas of thymic development²¹ (13) and individual signatures for CAR-T dysfunction³⁵ and CD28z tonic signaling⁵⁵ and are provided in the Supplementary Information.

scRNA-seq and CITE-seq analysis

scRNA-seq counts and associated metadata for Bai et al.³¹ and Haradhvala et al.³² were retrieved from the Gene Expression Omnibus (GSE197215 and GSE197268, respectively). Gene counts were normalized using Seurat (4.1.0), and cell type labels were assigned using ProjectTILs³³ (2.2.0) with the default scRNA-seq-based reference atlas of tumor-infiltrating lymphocytes. Differential expression analysis was implemented with Seurat using a Wilcoxon rank-sum test, followed by GSEA. ssGSEA scores were calculated using GSVA (1.40.1) and used without normalization as input features to the classifier. For CITE-seq-based immunophenotyping, we called each cell as positive/negative based on reference to the associated control antibody tag.

ssGSEA-based response classifier

ssGSEA scores corresponding to all gene signatures that were differentially enriched between CR and NR groups in Fraietta et al.¹⁸ (28, based on an FDR-adjusted $P < 0.05$) were used to build a logistic regression-based classifier of response status:

$$\log\left(\frac{p(CR)}{1-p(CR)}\right) = \beta_0 + \beta_1 \cdot ssGSEA_1 + \beta_2 \cdot ssGSEA_2 + \dots + \beta_N \cdot ssGSEA_N$$

wherein $p(CR)$ is the probability of complete response (versus non-response), and β_i are regression coefficients. A genetic algorithm, implemented in R with the gmlmulti package (1.0.8), was used for feature selection on the 60% training split of the data, using the Akaike information criterion (AIC) with model accuracy as the objective function. Model accuracy is defined as:

$$\text{Accuracy} = (TP + TN) / (TP + TN + FP + FN)$$

wherein TP, TN, FP and FN refer to true positive, true negative, false positive and false negative. For the genetic algorithm, we used a population size of 100 with a mutation rate of 0.001, an immigration rate of 0.3 and a reproduction rate of 0.1. Owing to the stochastic nature of genetic algorithms, this was repeated 2,500 times, wherein each iteration produced a list of N pathways to be used as features for logistic regression. For randomized control models, we randomly selected $2 \leq N \leq 6$ pathways from the remnant pathway compendium (7,520, FDR-adjusted $P > 0.05$) as input features, using an N distribution based on observed frequencies in the trained models. Predictive accuracy was assessed using the 40% test split of the data and model accuracy distributions compared via Wilcoxon rank-sum tests and visualized as kernel density estimates with manually chosen bandwidths. Immunophenotype classifiers were developed using the same workflow excluding feature selection, with input features being either reported cell frequencies from Fraietta et al.¹⁸ computed cell frequencies from Bai et al. CITE-seq data³⁴ or computed cell frequencies from ProjectTILs³³ annotation of Haradhvala et al.³² data.

Binomial tests were used to assess GSEA overlap in CR versus NR/PR/RL comparisons among datasets. Starting with the top 28 gene

signatures identified as differentially expressed in Fraietta et al.¹⁸ and used to seed the transcriptome classifier, 13/28, 13/28 and 15/28 are significant at a level of $P < 0.05$ in the Bai et al.³⁴ and Haradhvala et al.³² Kymriah and YesCarta datasets, respectively. Of the 7,548 signatures in our compendium, 1,123, 742 and 751 met this level of significance, corresponding to P values of 6×10^{-5} , 7×10^{-7} and 10^{-8} .

Software

Model simulations and analysis were performed using MATLAB R2021a and the SimBiology toolbox (6.1). All bioinformatics analysis was done on Ubuntu 20.04.3 LTS running R 4.1.1 ('Kick Things'). Key packages were GSVA (1.40.1) for ssGSEA, fgsea (1.21.2) for GSEA, celldex (1.2.0) for obtaining reference datasets for SingleR (1.6.1), Seurat (4.1.0), data.table (1.14.2), limma (3.50.3), edgeR (3.34.1), Matrix (1.4.3) and ggplot2 (3.3.6) for data wrangling and visualization.

Reporting summary

Further information on research design is available in the Nature Portfolio Reporting Summary linked to this article.

Data availability

Single-cell RNA sequencing counts and associated metadata for Bai et al.³¹ and Haradhvala et al.³² were retrieved from the Gene Expression Omnibus (GSE197215 and GSE197268, respectively). Bulk RNA sequencing and associated metadata from Fraietta et al.¹⁸ were downloaded from the supplement, and all additional data were digitized from published figures using Graph Grabber version 2 (Quintessa).

Code availability

The MATLAB and R code used in this study is provided for non-commercial use via a Zenodo repository: <https://doi.org/10.5281/zenodo.6886414> (ref. ⁵⁶).

References

45. Kalos, M. et al. T cells with chimeric antigen receptors have potent antitumor effects and can establish memory in patients with advanced leukemia. *Sci. Transl. Med.* **3**, 95ra73 (2011).
46. Restifo, N. P. & Gattinoni, L. Lineage relationship of effector and memory T cells. *Curr. Opin. Immunol.* **25**, 556–563 (2013).
47. Gesztelyi, R. et al. The Hill equation and the origin of quantitative pharmacology. *Arch. Hist. Exact Sci.* **66**, 427–438 (2012).
48. Boer, R. J. D. & Perelson, A. S. Towards a general function describing T cell proliferation. *J. Theor. Biol.* **175**, 567–576 (1995).
49. Boer, R. J. D. & Perelson, A. S. Quantifying T lymphocyte turnover. *J. Theor. Biol.* **327**, 45–87 (2013).
50. Martínez-Rubio, Á. et al. A mathematical description of the bone marrow dynamics during CAR T-cell therapy in B-cell childhood acute lymphoblastic leukemia. *Int. J. Mol. Sci.* **22**, 6371 (2021).
51. Sommer, C. et al. Preclinical evaluation of allogeneic CAR T cells targeting BCMA for the treatment of multiple myeloma. *Mol. Ther.* **27**, 1126–1138 (2019).
52. Stein, A. The cellular kinetics and anti-tumor dynamics of Kymriah. In AcoP10 (ISOP, 2019); https://drive.google.com/file/d/1Uz69ZXIVLp_9RPaBBhex7fLxRPk7og8e/view
53. Ritchie, M. E. et al. limma powers differential expression analyses for RNA-sequencing and microarray studies. *Nucleic Acids Res.* **43**, e47 (2015).
54. Barbie, D. A. et al. Systematic RNA interference reveals that oncogenic KRAS-driven cancers require TBK1. *Nature* **462**, 108–112 (2009).
55. Albert, S. et al. Tonic signaling and its effects on lymphopoiesis of CAR-armed hematopoietic stem and progenitor cells. *J. Immunol.* **202**, 1735–1746 (2019).

56. Kirouac, D., Zmurchok, C., Sicherman, J. & Deyati, A. Clinical variance in CAR-T pharmacology and response deconvoluted using a mathematical model of T cell regulatory control. Preprint at Zenodo <https://doi.org/10.5281/zenodo.6886414> (2022).

Acknowledgements

We would like to thank I. Elliott Donaghue, G. Block, M. Bellew and S. Chandrasekaran for review of the manuscript and helpful commentary; C. Mullins for project management support; and A. Stein for discussions on population modeling of Kymriah.

Author contributions

D.C.K. devised and directed the project. D.C.K. and C.Z. performed the mathematical modelling and subsequent analysis. A.D. and J.S. performed the bioinformatics and machine learning analyses. D.C.K. and C.Z. wrote the manuscript, with input from all authors. P.W.Z. and C.B. contributed to the interpretation of the results and direction of work. All authors provided ideas and critical feedback, helping shape the research strategy, analysis, figure preparation and writing.

Competing interests

All authors are employees and/or shareholders of Notch Therapeutics, but they declare no competing financial interests and received no specific funding for this work.

Additional information

Supplementary information The online version contains supplementary material available at <https://doi.org/10.1038/s41587-023-01687-x>.

Correspondence and requests for materials should be addressed to Daniel C. Kirouac.

Peer review information *Nature Biotechnology* thanks Luciana Barros and the other, anonymous, reviewer(s) for their contribution to the peer review of this work.

Reprints and permissions information is available at www.nature.com/reprints.



Deconvolution of clinical variance in CAR-T cell pharmacology and response

In the format provided by the
authors and unedited

Supplemental Information

Review of published CAR-T pharmacokinetic/pharmacodynamic models

Chaudry et al.¹ have described a taxonomy of CAR-T cell kinetic models, proposing a few requisite properties:

1. Capture the typical 3 phase pharmacokinetic profiles – exponential expansion, rapid decline, then long term decay.
2. CAR-T expansion is driven by antigen – multiple clinical and pre-clinical observations note that expansion (Cmax) correlates with initial tumor burden.
3. CAR-T cell expansion is limited – insufficient cell doses are incapable of clearing the tumor.
4. Absence of limit cycles – many models predict oscillations of CAR-T and tumor cell numbers, which have not been observed clinically nor in pre-clinical models.

The ‘gold-standard’ pharmacokinetic model published by Stein et al.² and now used by the FDA is purely empirical. It describes CAR-T pharmacokinetics (property 1), but does not include tumor dynamics, thus falls short of properties 2 and 3.

Published mechanism-based models are all derivatives of the predator-prey formulation³, wherein tumor (antigen) stimulates T cell proliferation, and T cells in turn kill tumor cells, satisfying property 2 by design. However, in all published variants, T cells are endowed with unlimited proliferative capacity; limited only by the loss of tumor (the growth of T cells follows a mass-action law dependent on T cells and tumor cells). As such, a single infused CAR-T cell, given time to expand, will eventually clear tumor^{4–6}, thereby missing property 3. Predator-prey models are also prone to limit cycles (e.g., Martinez-Rubio et al.⁴). Oscillations are theoretically possible in many feedback-regulated dynamical systems, and clinically manifest in rare cyclic hematological disorders⁷. However, oscillations in either circulating CAR-T or tumor cell counts have not been reported to our knowledge in any pre-clinical or clinical data, though these could be missed due to sampling limitations and patient variability.

Two approaches have been taken to enable predator-prey model formulations to address properties 2 and 3. Singh et al.^{8,9} implement a predator-prey model, but encode CAR-T proliferation using a Hill-equation driven by CAR:Antigen complexes per tumor cell, such that low CAR-T doses deliver insufficient receptor to breach this threshold^{8,9}. The dose-response simulations thereby display a switch-type behavior with respect to both CAR-T exposure and tumor response: cell doses below a given threshold result in minimal CAR-T expansion or tumor response, and those above result in complete response, with time-to-Cmax being dose-responsive. While this (partially) addresses requisite properties 3 and 4, it suggests that complete responses can be achieved by simply dosing above the threshold and does not explain the observed clinical variability. Moreover, it necessitates an estimate of CAR expression on T cells and antigen expression on tumor tissue, as well as in vitro data to parameterize the relationship between CAR:antigen formation, T cell proliferation and cytotoxicity.

The model published by Kimmel et al.¹⁰ is predator-prey based, but also implements competition between host T cells and CAR-Ts for limited ‘space’, thereby limiting CAR-T expansion. In this model the *a priori* differentiating factor between patients with robust CAR-T expansion (and tumor clearance) vs. poor CART expansion (and tumor progression) is the kinetics of host immune system reconstitution. This hypothesis is supported by clinical data on the role of lymphodepletion in mediating CAR-T expansion and efficacy¹¹. However, it does not preclude the involvement of alternate, product-intrinsic mechanisms in limiting cell expansion and underlying patient-to-patient variability.

Our model formulation makes a few fundamental changes to the typical predator-prey structure to address the four requisite properties and incorporate fundamental T cell biology. Borrowing from the stem cell field, we encode each T memory (T_M) cell division as a fate choice between self-renewal and differentiation, driven by tumor antigen (B_A). CAR-T differentiation and expansion thus occur at the expense of depleting the pool of memory cells. Effector cells (T_E) cannot self-renew, but rather undergo a fixed number (N) of divisions. This is a novel feature absent from other mechanism-based CAR-T models and addresses the unlimited CAR-T expansion capacity embedded in predator-prey models. Accounting of memory cell self-renewal vs. differentiation also provides a mechanism by which chronic antigen stimulation (or alternatively, insufficient CAR-T dose relative to tumor size) drives exhaustion. If tumor cells cannot be cleared sufficiently to reduce systemic antigen burden below a defined threshold (B_{50}), T_M cells will continually differentiate until the pool of long-term memory cells is depleted.

We have also included an exhausted T cell state, notably absent from all above CAR-T models. We believe this is necessary to capture the divergence between CAR-T pharmacokinetics and cytotoxic function, particularly in partial and non-responding patients (explored in detail below).

Model structural assessment

To systematically assess the model topology, we created a series of variants with alternate T cell population structures:

1. T_E population only (effector state)
2. T_M and T_E (memory and effector states), no T_X
3. T_E and T_X (effector and exhausted states)
4. T_M , T_E , and T_X states, but without effector to memory differentiation ($r_M = 0$)
5. Inclusion of additional naïve (T_N) state to the original model.

We illustrate these model structures as cartoons in **Figure S1**.

Note the original (complete model) describes 4 sub-populations regulated by antigen exposure via the ODEs:

$$\begin{aligned} \frac{dT_M}{dt} &= \mu_M \cdot \left(2 \cdot f_{max} \cdot \left(1 - \frac{B_A^{km}}{B_{50}^{km} + B_A^{km}} \right) - 1 \right) \cdot T_M + r_M \cdot \left(1 - \frac{B_A^{kr}}{B_{50}^{kr} + B_A^{kr}} \right) \cdot T_{E2} - d_M \cdot T_M, \\ \frac{dT_{E1}}{dt} &= 2 \cdot \mu_M \cdot \left(1 - f_{max} \cdot \left(1 - \frac{B_A^{km}}{B_{50}^{km} + B_A^{km}} \right) \right) \cdot T_M - \mu_E \cdot \left(\frac{B_A^{ke}}{B_{50}^{ke} + B_A^{ke}} \right) \cdot T_{E1} - d_{E1} \cdot T_{E1} \\ \frac{dT_{E2}}{dt} &= \mu_E \cdot 2^N \left(\frac{B_A^{km}}{B_{50}^{km} + B_A^{km}} \right) \cdot T_{E1} - k_{ex} \left(\frac{B_A^{kx}}{B_{50}^{kx} + B_A^{kx}} \right) \cdot T_{E2} - r_M \cdot \left(1 - \frac{B_A^{kr}}{B_{50}^{kr} + B_A^{kr}} \right) \cdot T_{E2} - d_{E2} \cdot T_{E2} \\ \frac{dT_X}{dt} &= k_{ex} \left(\frac{B_A^{kx}}{B_{50}^{kx} + B_A^{kx}} \right) \cdot T_{E2} - d_X \cdot T_X. \end{aligned}$$

For model **variant 1**, we describe the single effector compartment, wherein proliferation/self-renewal is driven by antigen:

$$\frac{dT_{E2}}{dt} = \mu_E \left(\frac{B_A^{km}}{B50^{km} + B_A^{km}} \right) \cdot T_{E2} - d_{E2} \cdot T_{E2},$$

For model **variant 2**, we employ the full model, but set $k_{ex} = 0$ such that no exhausted T cells are generated.

For model **variant 3**, we employ a version of variant 1, wherein effectors both proliferate/self-renew and transit to exhausted cells in an antigen-dependent manner.

$$\frac{dT_{E2}}{dt} = \mu_E \left(\frac{B_A^{km}}{B50^{km} + B_A^{km}} \right) \cdot T_{E2} - k_{ex} \left(\frac{B_A^{kx}}{B50^{kx} + B_A^{kx}} \right) \cdot T_{E2} - d_{E2} \cdot T_{E2}$$

$$\frac{dT_X}{dt} = k_{ex} \left(\frac{B_A^{kx}}{B50^{kx} + B_A^{kx}} \right) \cdot T_{E2} - d_X \cdot T_X.$$

For model **variant 4**, we employ the original set of model equations, but set $r_M = 0$ such that memory cells cannot arise from effectors. Note the origin of long-term memory cells remains a point of contention among immunologists. It is established that following clearance of infection, antigen-specific effectors are replaced by antigen-specific memory cells. These were previously assumed to arise via de-differentiation from a subset of differentiation effectors ¹² (as coded in our model), though new evidence suggests that these arise from a rare population of stem-like cells ¹³. There is data supporting both lineage models ^{14,15}, and differing sub-sets of memory cells may follow both paths ^{16,17}. This variant thus assesses whether this teleological de-differentiation reaction is necessary within our model framework, given the limited number of T cell states considered for parsimony.

For model **variant 5**, we have included a naïve T cell compartment (T_N) preceding the memory compartment, as per canonical T cell differentiation hierarchy ¹². These cells proliferate and differentiate to memory T_M cells in an antigen-dependent manner, via the equation:

$$\frac{dT_N}{dt} = 2 \cdot \mu_N \cdot f_N \cdot \left(1 - \frac{B_A^{kn}}{B50^{kn} + B_A^{kn}} \right) \cdot T_N - d_N \cdot T_N$$

T_N cells differentiate into the memory cell compartment, such that the T_M balance equation is now:

$$\begin{aligned} \frac{dT_M}{dt} = & \mu_M \cdot \left(2 \cdot f_{max} \cdot \left(1 - \frac{B_A^{km}}{B50^{km} + B_A^{km}} \right) - 1 \right) \cdot T_M + 2 \cdot \mu_M \cdot f_{max} \cdot \left(1 - \frac{B_A^{km}}{B50^{km} + B_A^{km}} \right) \cdot T_M + r_M \\ & \cdot \left(1 - \frac{B_A^{kr}}{B50^{kr} + B_A^{kr}} \right) \cdot T_{E2} - d_M \cdot T_M \end{aligned}$$

This introduces five additional free parameters into the model:

μ_N : the naïve T cell proliferation rate

f_N : the naïve T cell probability of self-renewal

k_N : the Hill exponent linking antigen exposure to naïve T cell proliferation

d_N : the naïve T cell death rate

fraction_T_N: the fraction of CAR-T cell dose in the naïve T cell compartment

The resulting model fits to the CR/PR/NR populations from Fraietta et al.¹⁸ for the five structural variants as compared to the full model are shown in **Figure S2**. Note that all model variants are essentially equivalent with respect to their ability to describe the tumor dynamics but differ substantially in the ability to capture the CAR-T pharmacokinetics.

Model selection for non-linear dynamical models is inherently challenging given the lack of appropriate quantitative metrics. The Akaike Information Criterion (AIC) is widely used, ranking models based on fitting error (MSE) vs. complexity (number of free parameters):¹⁹:

$$AIC = n \cdot \ln[MSE] + \frac{2 \cdot k \cdot n}{n - k - 1}$$

Wherein n = number of measurements, k = free parameters and MSE = mean squared error.

However, this was originally developed to rank multivariate linear regression models rather than non-linear ODEs and prioritizes limiting free parameters over goodness-of-fit. More fundamentally, MSE essentially considers all data points to be of equivalent value, while subjectively we know some datapoints and readouts are more-or-less significant. Given the tumor dynamic profiles look quite similar across variants, we reasoned tumor fits are not important model selection criterion. The most clinically relevant criteria is efficacy, and CAR-T exposure metrics (Cmax and AUC) are known to predict clinical efficacy. We thus evaluated all model variants by MSE of the Cmax (log10-cells) and AUC (log10-cells.day) in addition to the MSE of all the data and the sample-size corrected AIC:

Variant	Parameters (k)	MSE (all data)	AICc (all data)	MSE (CART Cmax)	MSE (CART AUC)
0	27	0.148	56.94	0.023914	701.89
1	12	1.477	51.31	0.238173	2633451.7
2	23	0.194	24.82	0.12383	1777.4
3	18	1.398	77.38	0.283941	1969201.3
4	26	0.241	66.01	0.458429	2322.9
5	32	0.052	140.4	0.059707	850.18

*bold indicates top ranked model by metric

Based on MSE of all the data, variant 5 (inclusion of the T_N cell compartment) is the most accurate, outperforming the original model (variant 0). Examination of the PK curves in **Figure S1** reveals this improvement is due to capturing the last time point (12 month) of the NR profile, which increases from the previous (6 month). We believe this may be an artefact of the data (population average) rather than a real phenomenon, implying the model is overfitting. Note that model variant 5 contains five additional parameters as compared to the original model, and the resulting AIC more than doubles from 57 to 140, indicating this additional complexity adds little value.

Based on the AICc, variant 2 (lacking an exhausted state but containing T_M and T_E , and the reversible transitions) is ranked highest. However, this version does not adequately capture the pharmacokinetics of the NR population, which reads out as higher MSE of the CAR-T exposure metrics (Cmax and AUC). The deficiency of using AICc as a model selection metric is apparent by examining the curves for model variant 1 (lacking T_M and T_X compartments). While this is ranked higher than the original model due to the reduced number of free parameters, the PK curves do not even closely resemble the data.

Using the exposure metrics (both Cmax and AUC), the original model (variant 0) best captures the data. Consideration of the fitting error, model complexity, and assessment of exposures, we feel the original model outperforms all structural variants.

Note that selection of non-linear models is somewhat subjective. We view mathematical models as caricatures of biological systems; quantitative tools that should capture dynamic organizing principles and explain the data in broad strokes. A model's value lies in what we can learn from it, rather than how

complex and detailed it is. That is, the different variants assessed (and perhaps others not considered) could be equally valuable. These fitting metrics help decide which models to learn from, but do not necessarily imply one as true and others false.

Supplemental Figures

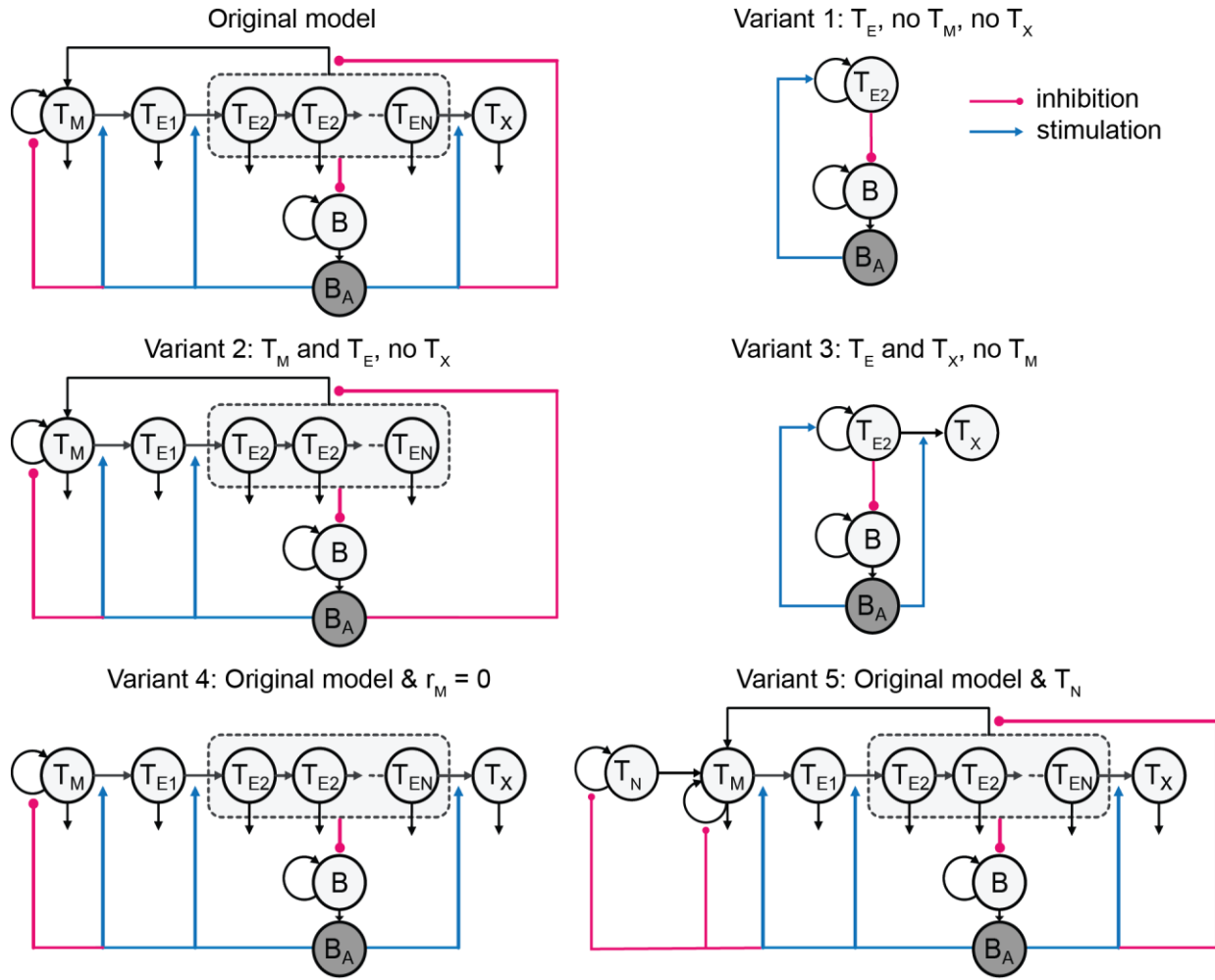


Figure S1: Structures of original model and variants.

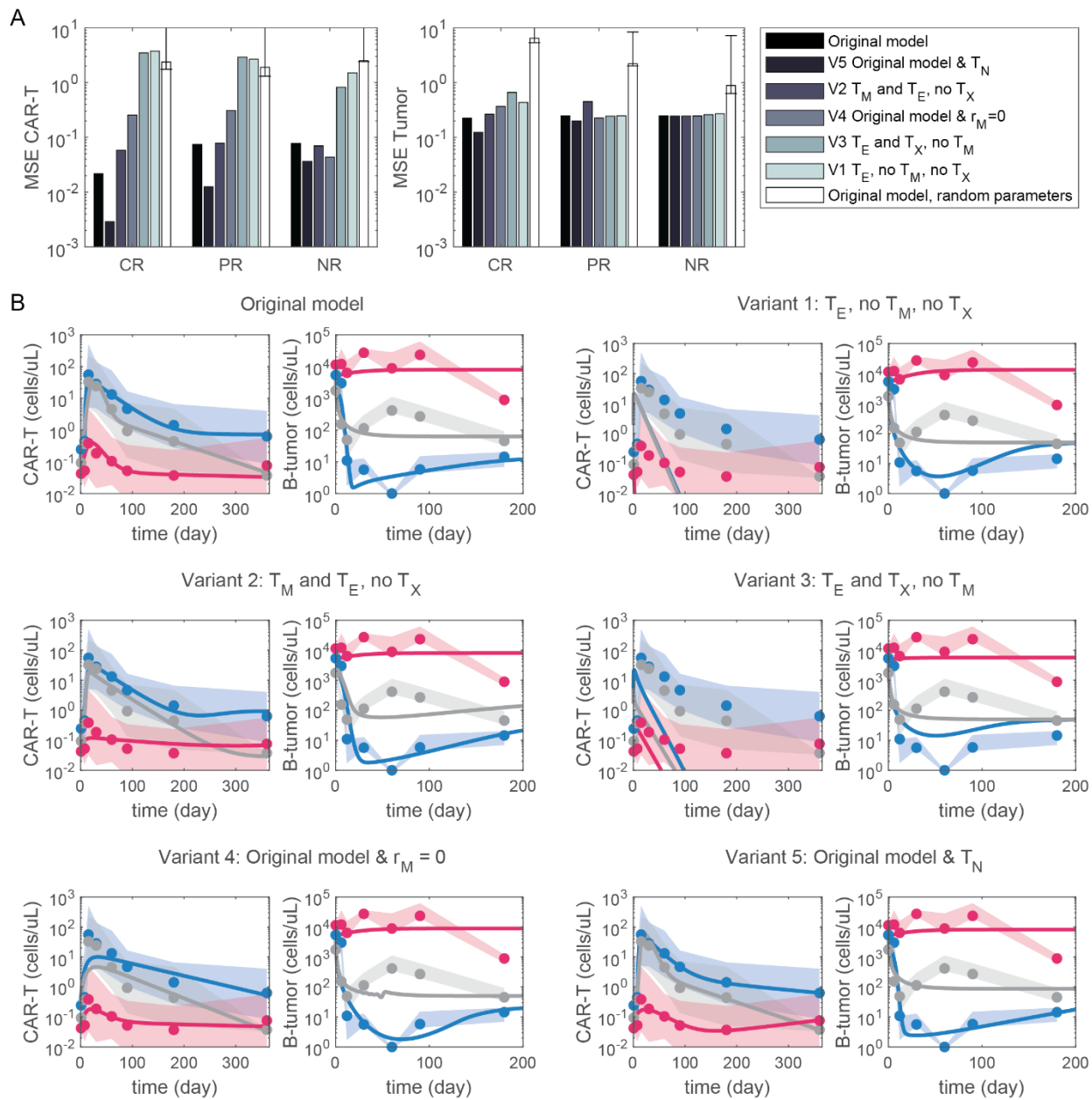


Figure S2: Fitting accuracy of the original proposed model against five structural variants. (A) Mean squared error (MSE) of the original (full) model and the five model variants fit the training data¹⁸, as well as random sampling of parameter search space for the original model ($n=100$, error bars = std). MSE plots are separated by fit to the pharmacokinetic and tumor dynamics, and rank ordered by overall goodness of fit. (B) Model simulations overlaid with training data for the original (full) model and five variants.

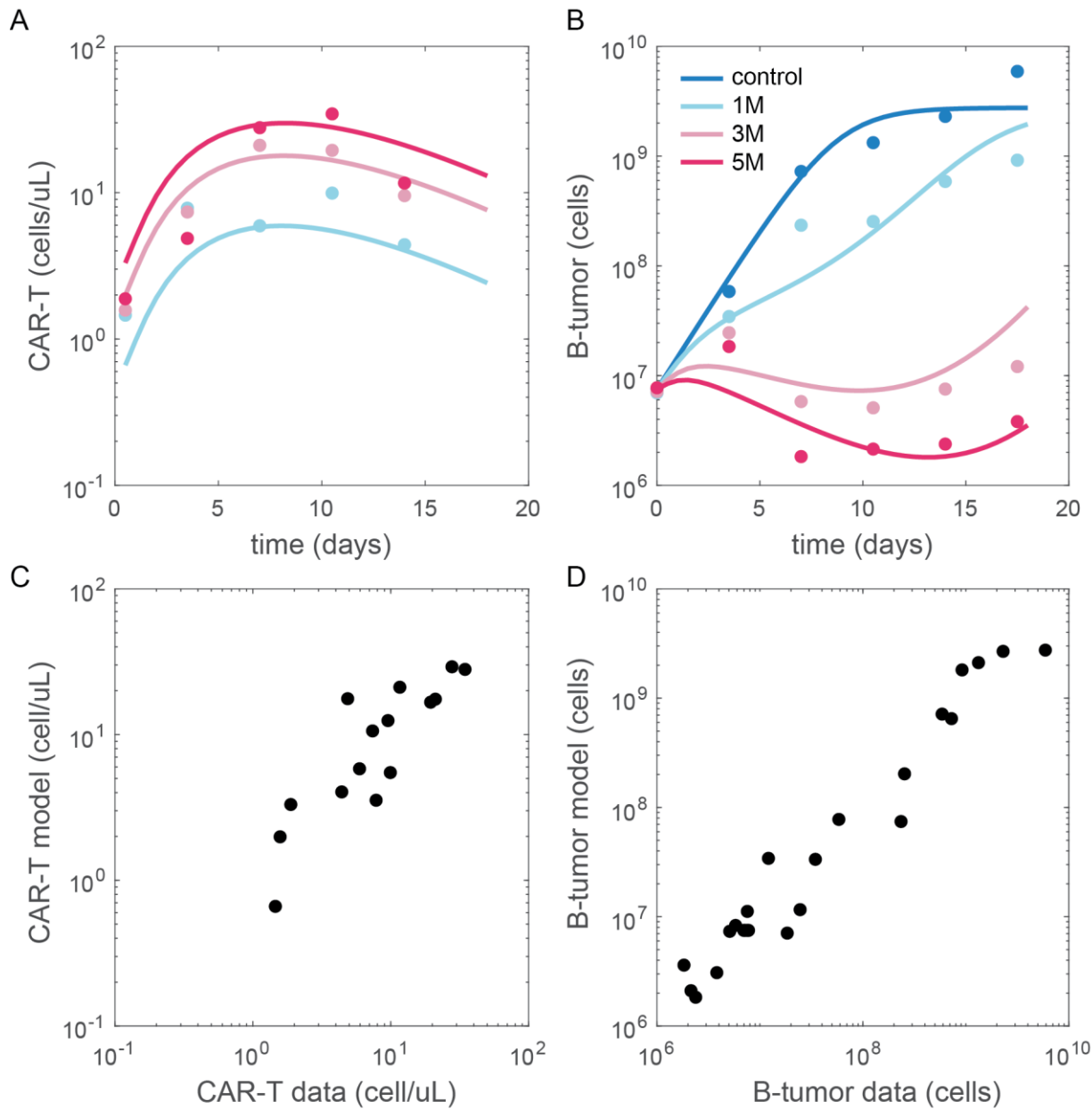


Figure S3. Model fitting to pre-clinical CD19-CAR-T data. NALM-6 xenograft bearing mice (injected with 106 tumor cells at day -6) were treated with increasing doses of Kymriah, and tumor size measured by fluorescence imaging²⁰. We assume for simplicity a 1:1 scaling relationship between photons/s and tumor cell number. For fitting mouse as compared to clinical data, we scaled down bounds on the tumor-related parameters Bmax (maximum tumor size) and TK50 (T cell EC50 driving tumor cell killing) and allowed the tumor growth rate (μ_B) to float between 0.1 and 1 per day. (A) Pharmacokinetic and (B) tumor dynamic data and model simulations for CAR-T doses of 0, 1, 3 and 5 million cells. Goodness of fit plots for the CAR-T pharmacokinetic (C) and tumor dynamics (D), with Pearson correlation coefficients of 0.88 and 0.84 respectively.

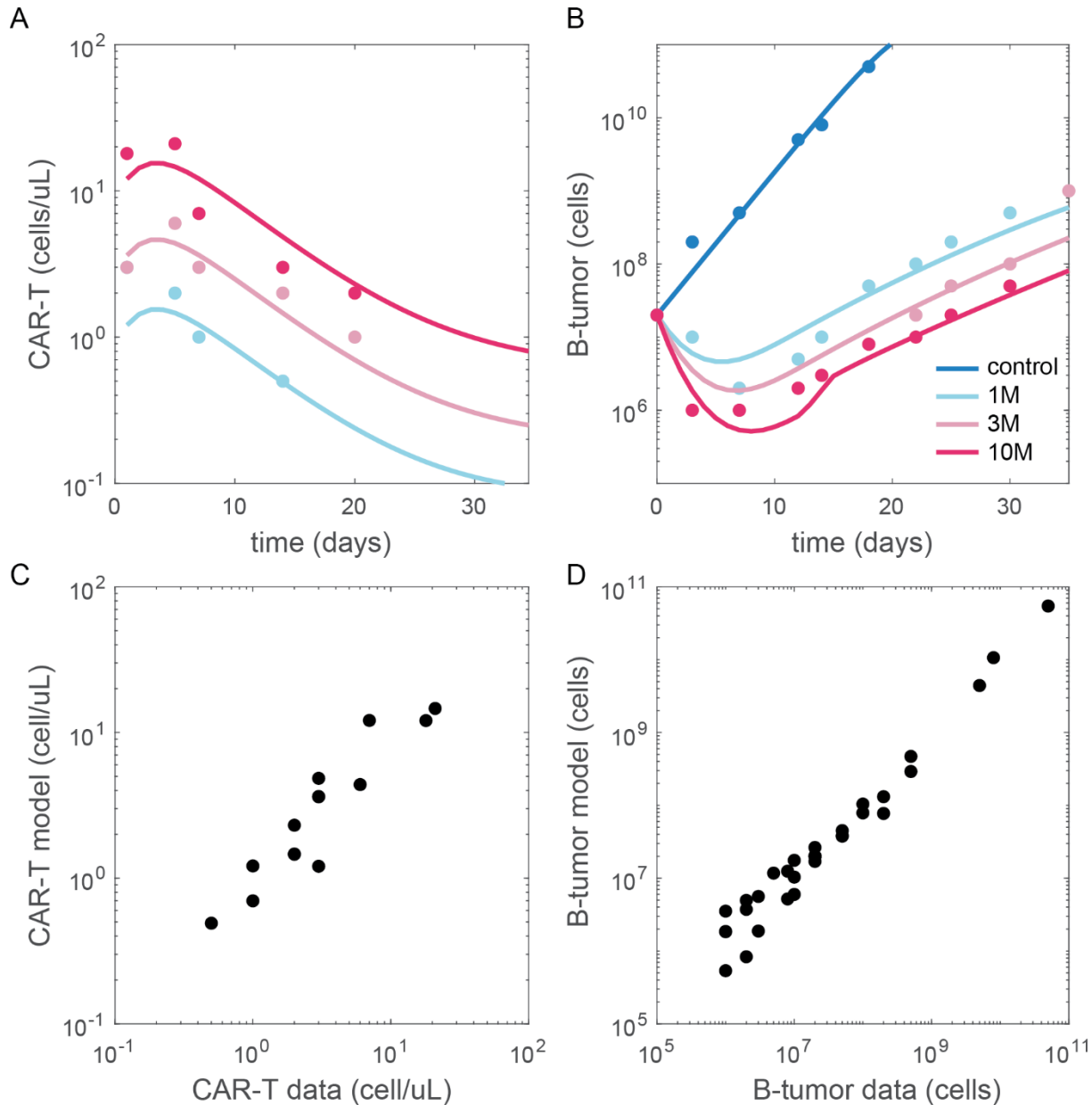


Figure S4. Model fitting to pre-clinical BCMA-CAR-T data. MM1.s xenograft bearing mice (injected with 5×10^6 tumor cells at day -14 to -8) were treated with increasing doses of the research-grade CAR-T ‘BCMA-R2’, and tumor size measured by fluorescence imaging²¹. We assume for simplicity a 1:1 scaling relationship between photons/s and tumor cell number. For fitting mouse as compared to clinical data, we scaled down bounds on the tumor-related parameters B_{max} (maximum tumor size) and $TK50$ (T cell EC50 driving tumor cell killing) and allowed the tumor growth rate (uB) to float between 0.1 and 1 per day. (A) Pharmacokinetic and (B) tumor dynamic data and model simulations for CAR-T doses of 0, 1, 3 and 10 million cells. Goodness of fit plots for the CAR-T pharmacokinetic (C) and tumor dynamics (D), with Pearson correlation coefficients of 0.92 and 0.99 respectively.

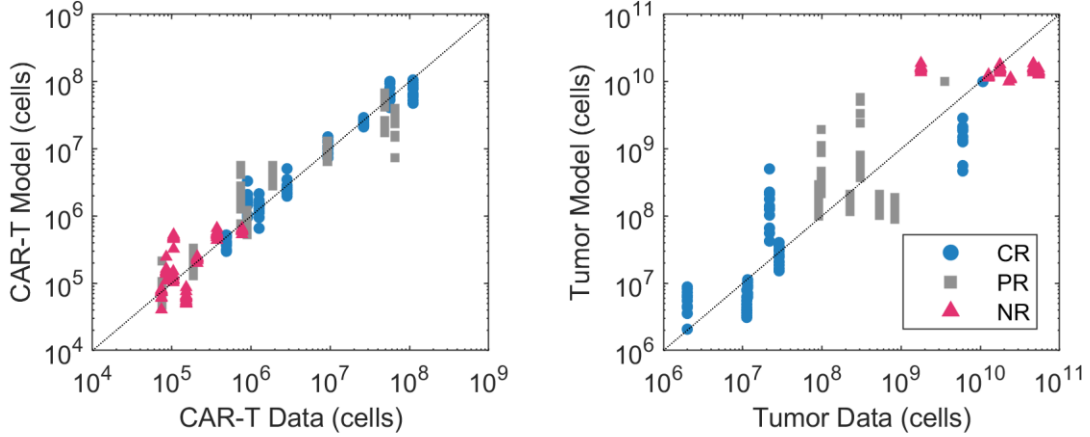


Figure S5: Goodness-of-fit plots for Kymriah model fitting in Figure 1. Accuracy was quantified by computing Pearson correlations of the goodness-of-fits (log-simulations vs. log-data), separated by CAR-T and tumor kinetics for the CR, PR, and NR populations. For the CAR-T pharmacokinetics, median correlation coefficients for the CR, PR, and NR populations are 0.89, 0.88, and 0.76, respectively. The model therefore captures the majority of variance in the PK data for all three groups. For tumor dynamics, the correlations are 0.78, 0.77, and -0.23, respectively. Note the tumor growth portion of the model is very minimal (logistic equation) and captures the overall trends and differences between populations while missing aspects of the dynamics. The CR tumor kinetics are captured relatively well. For the PR and NR groups, the model describes the dynamics of initial tumor size reduction (or lack thereof), but is not the subsequent dynamics. Both the PR and NR tumor dynamics appear to fluctuate up to day-100, then decline, though these may represent sampling artifacts rather than real dynamic features.

We further quantified accuracy by compared the mean squared errors resulting from the set of estimated model parameters to that obtained by random sampling of parameter search space ($n=100$). P -values for the three groups were all $< 10^{-7}$ (rank-sum test), indicating the optimized parameters represent a small segment of parameter space.

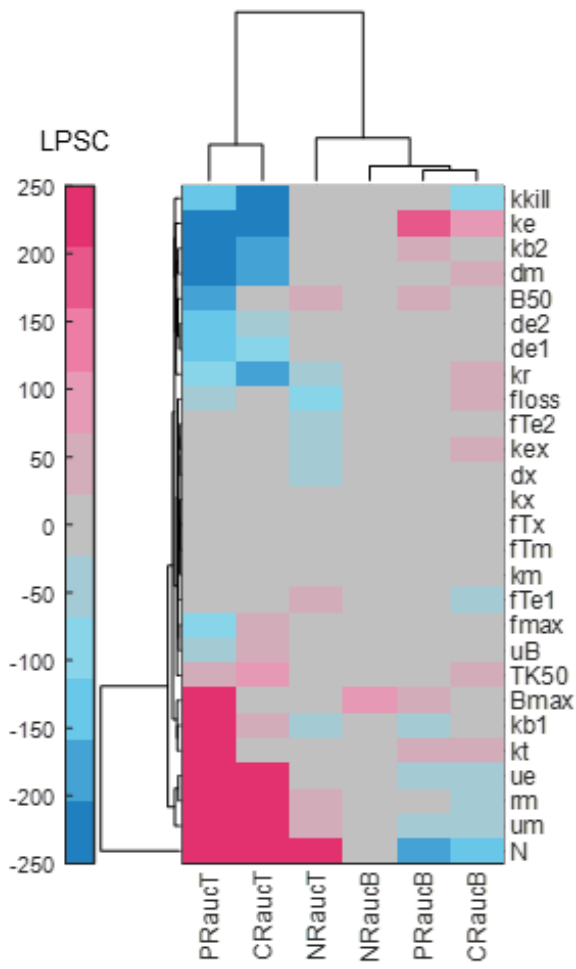


Figure S6: Local Parameter Sensitivity Analysis of CR/PR/NR populations. Local Parameter Sensitivity Coefficients (LPSC) were calculated for CR, PR, and NR populations using the AUC of T cells (aucT) and AUC of B cells (aucB) as outputs, with samples and outputs organized by agglomerative hierarchical clustering. Memory cell proliferation (μ_M) was identified as a critical driver of exposure and response in the CR and PR populations. TK50 was not a locally sensitive parameter despite being identified in the PCA as an important parameter (Figure 1D). The rate of tumor cell lysis (k_{kill}) was the most sensitive parameter mediating tumor response in the CR population. The rate of memory cell regeneration (r_M) and the number of effector cell doublings (N) were additionally found to mediate both CAR-T exposure and tumor response in CR and PR populations, despite not varying significantly between the groups.

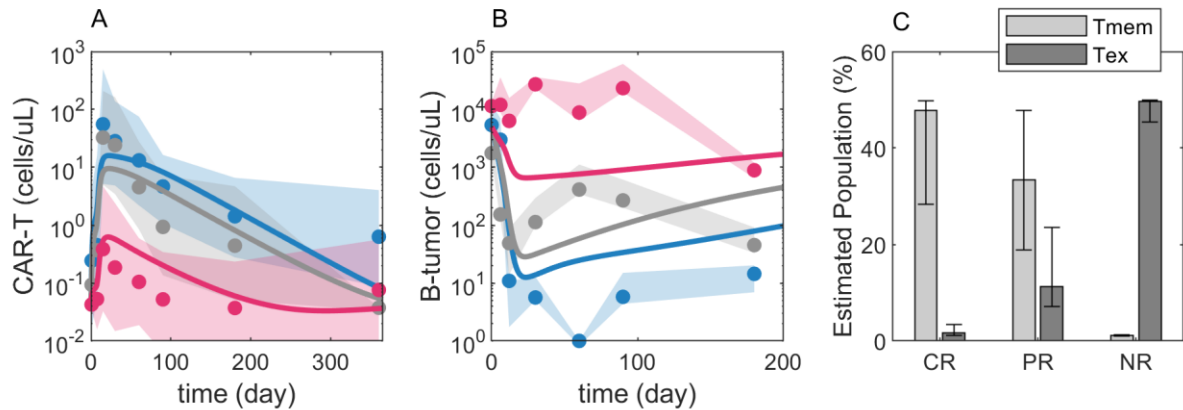


Figure S7. Model fitting results based on the hypothesis that the only distinguishing feature between CR, PR, and NR populations is the fraction of memory T and exhausted T cells in the CAR-T infusion product. Memory cell fraction (f_{Tm}) and exhausted cell fraction (f_{Tx}) were estimated as between 1-50% independently for the CR, PR, and NR populations while all other model parameters were estimated simultaneously using a single vector for the CR, PR, and NR populations. Simulations of best fit model (estimated by MSE minimization) from 12 optimization runs for (A) CAR-T pharmacokinetics and (B) tumor dynamics. (C) Estimated fraction of memory and exhausted cells (f_{Tm} , f_{Tx}) in CAR-T infusion products for CR, PR, and NR populations. Bars represent medians \pm 25 percentile intervals from n=12 model fits.

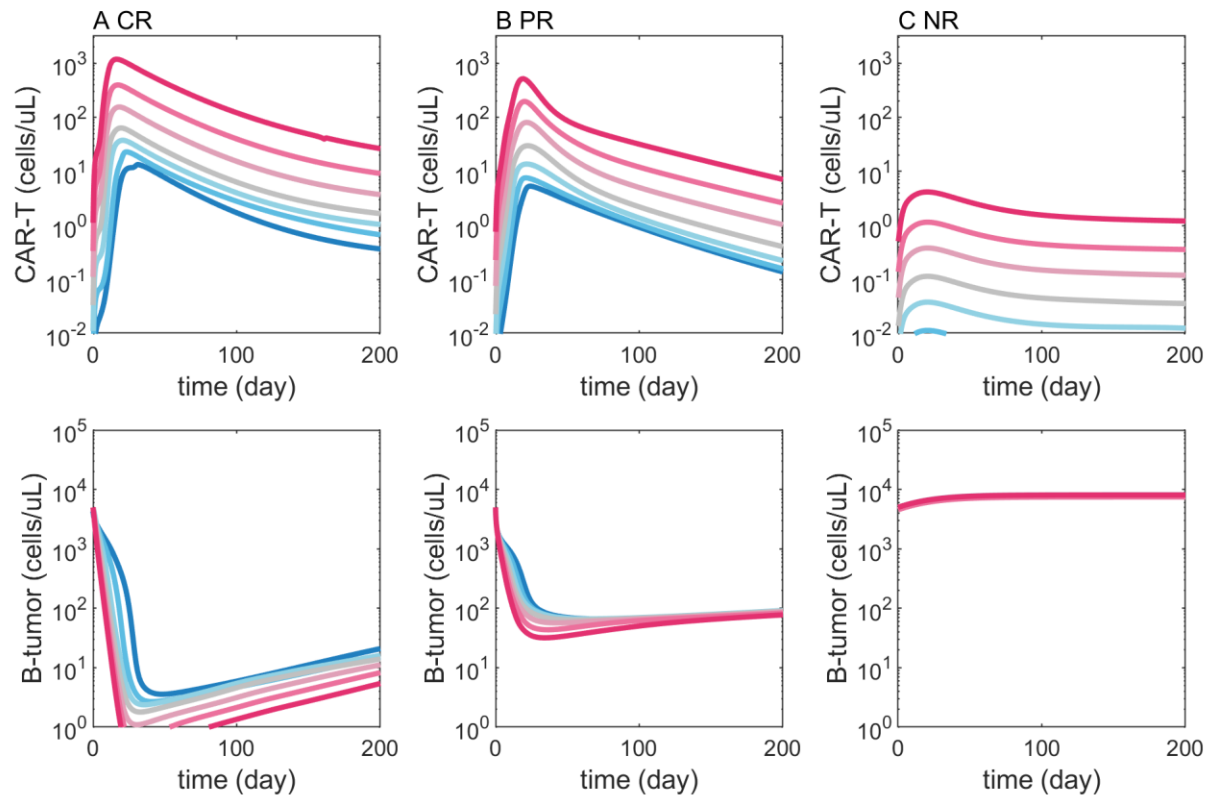


Fig S8. Simulated pharmacokinetic and tumor dynamic responses to increasing cell doses of pure memory cell populations from CR, PR, and NR population models. Simulations were run at doses of 1, 3, 10, 30, 100, 300 and 1000 million cells using parameter sets estimated for CR (A), PR (B), and NR (C) populations. For direct comparison, the memory cell fraction was set to 100% for each.

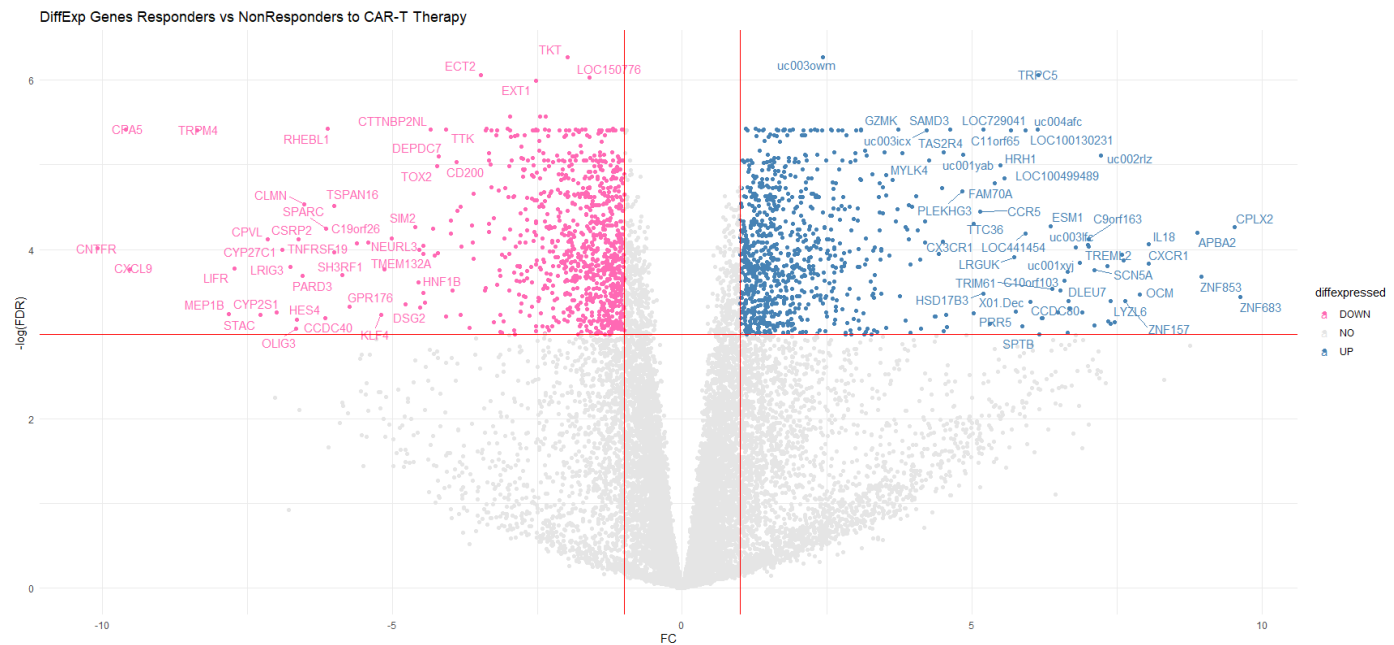


Figure S9. Volcano plot of differentially expressed genes between CR vs. NR groups. False-discovery Rate (FDR) based on moderated t-test in Limma.

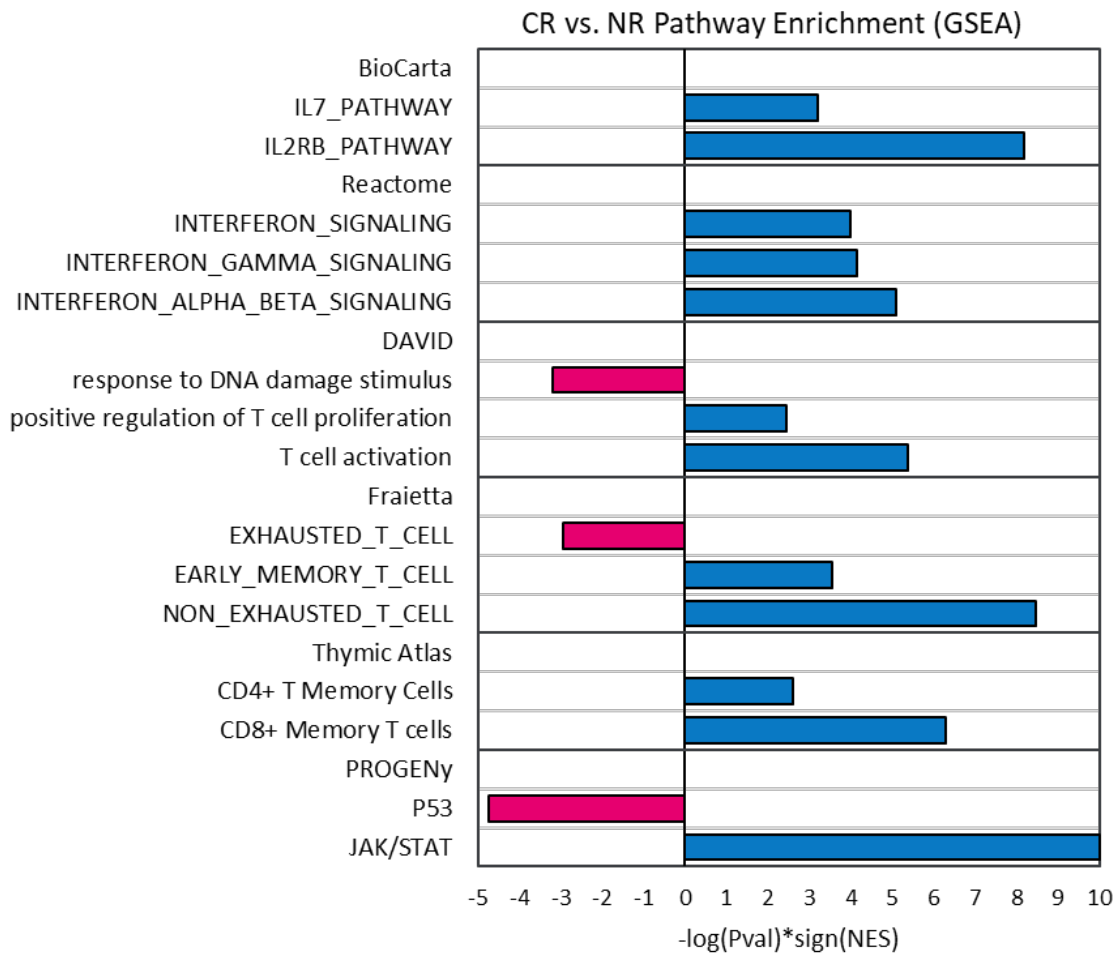


Figure S10. Select gene sets differentially enriched between CR vs. NR groups. Gene sets were derived from BioCarta, Reactome, DAVID, Fraietta et al., Thymic Cell Atlas and PROGENy, and represented as signed $\log_{10}(P\text{-val})$ P-values calculated using Kolmogorov-Smirnov test in GSEA.

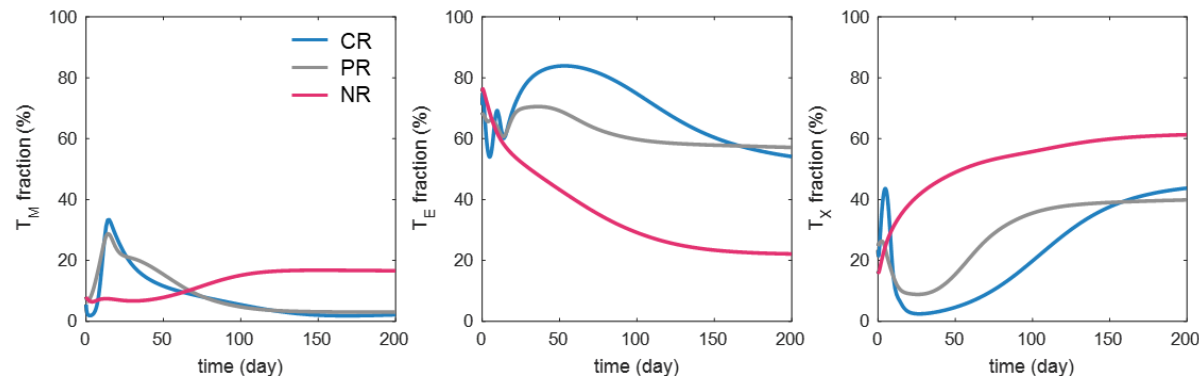


Figure S11. Simulated frequencies of memory (T_M), effector (T_E), and exhausted (T_X) CAR-T cells for CR, PR, and NR patient groups shown in Figure 1.

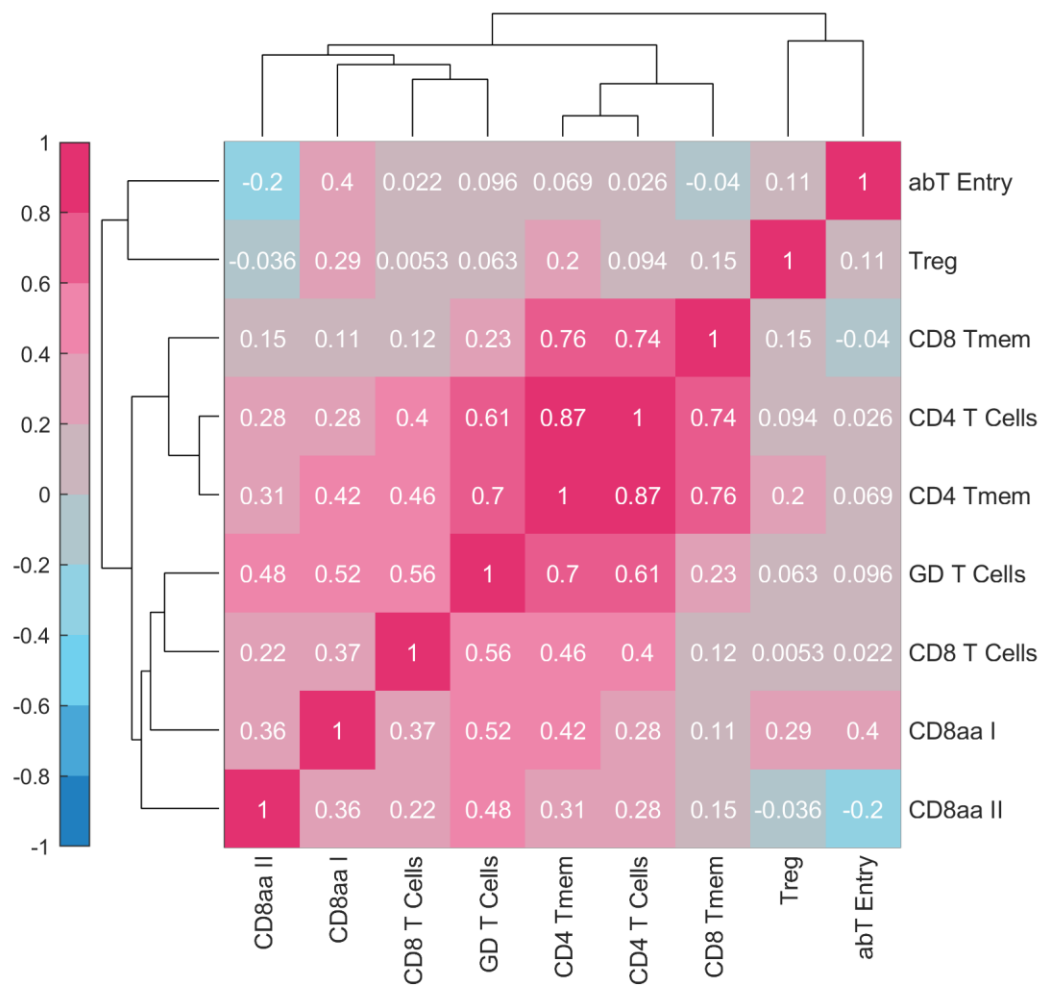
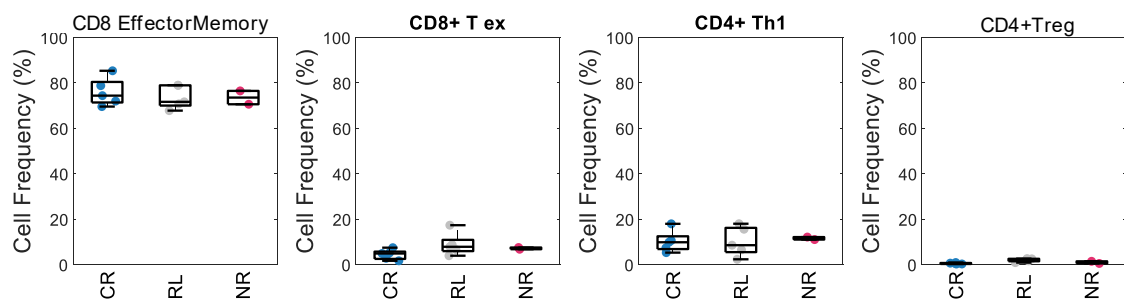
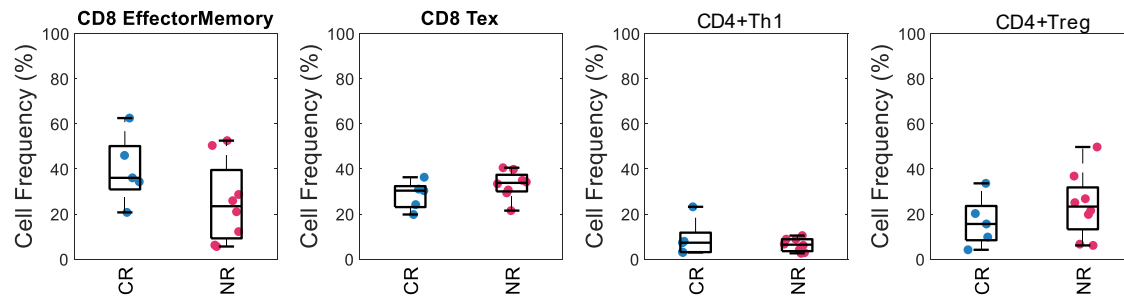


Figure S12. Pairwise Pearson correlation coefficients between Thymic Atlas cell population gene signatures computed using ssGSEA scores from Fraietta et al. RNAseq data. Note signatures for CD8 Tmem, CD4 Tmem, and CD4 T cells are tightly correlated.

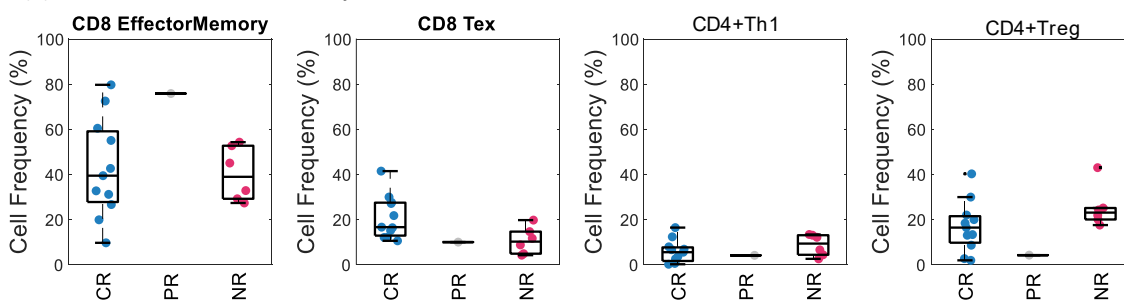
(A) Bai et al. ProjectTILs



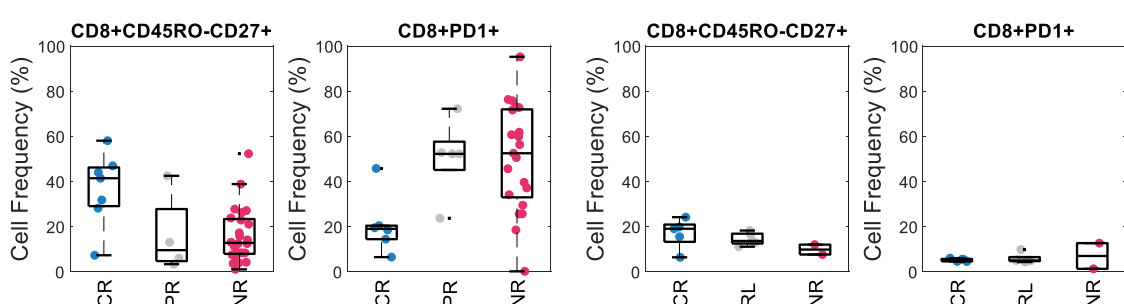
(B) Haradvala et al. Kymriah ProjectTILs



(C) Haradvala et al. Yescarta ProjectTILs



(D) Fraietta et al. Digitized



(E) Bai et al. CITESeq

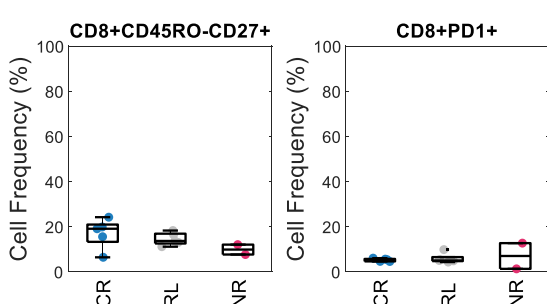


Figure S13: T cell phenotyping of CAR-T infusion products. ProjectTILs-annotated cell frequencies by response category for (A) Kymriah in ALL²², n=12; (B) Kymriah in LBCL²³, n=11; (C) Yescarta in LBCL²³, n=19. Cell types annotated at frequencies of less than 5% are excluded; CD4+ Naïve, CD8+ Naïve, CD8+ Tprecursor-exhausted (Tpex) and CD4+ follicular-helper (Tfh). (D) Immunophenotype-defined T early memory (CD8+CD45RO-CD27+) and exhausted (CD8+PD1+) cell frequencies by response category for Kymriah in CLL, digitized from Fraietta et al.¹⁸, n=38. (B) Immunophenotype-defined Early memory and exhausted cell frequencies by response category for Kymriah in ALL, calculated from Bai et al.²² CITEseq antibody tags, n=12. Boxplots represent median \pm 25 percentiles, and whiskers the min/max value or an additional 1.5-fold quartile distance.

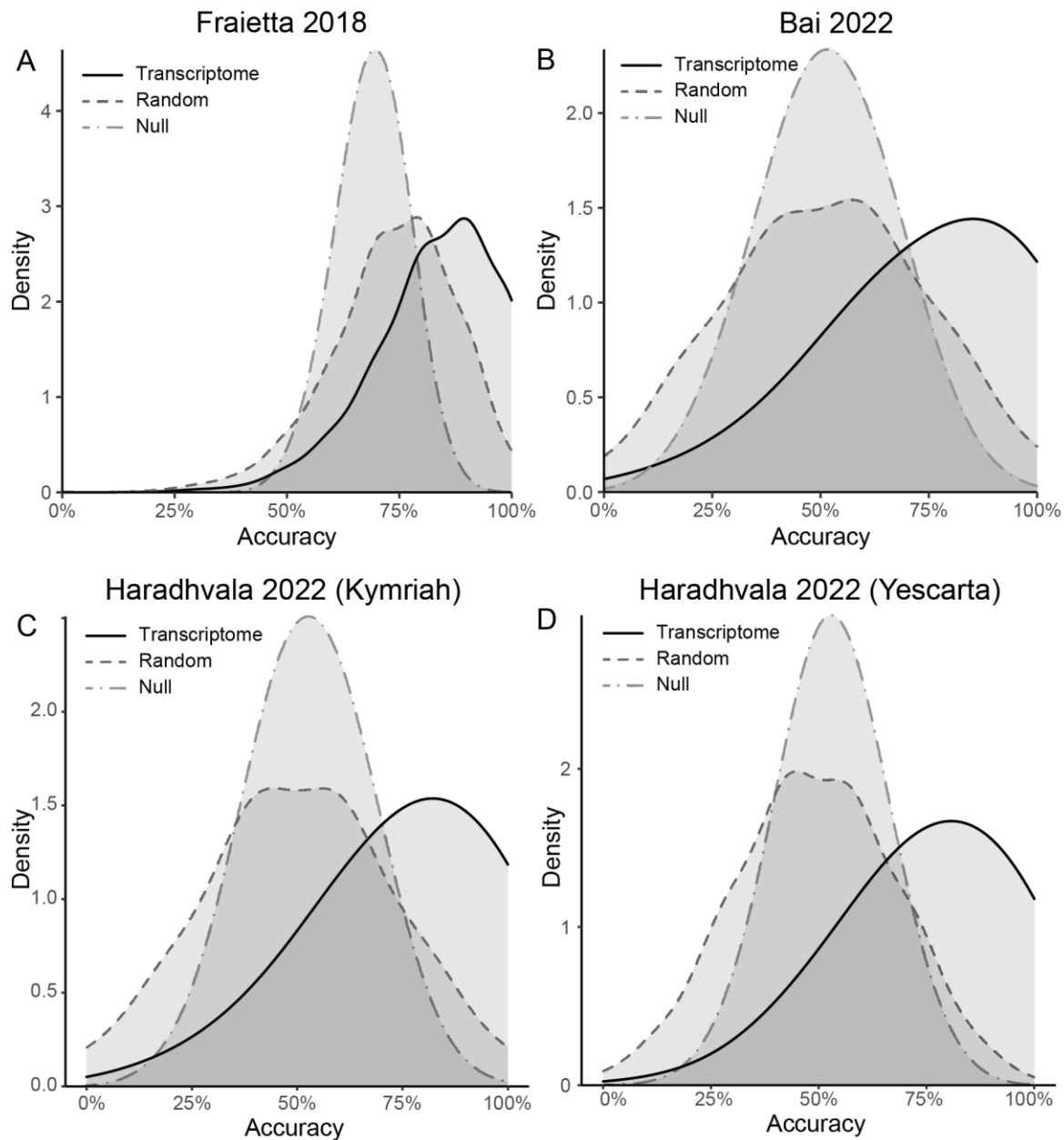


Figure S14: Transcriptome classifier performance as compared to null and random pathway models. Distribution of predictive accuracies are shown for 2500 iterations using 60:40 train:test split cross validation. Results from the 28-signature transcriptome-based ssGSEA classifier (“Transcriptome”) are compared null models (random classification; “null”) and an ssGSEA classifier trained on a randomized selection of pathways from the compendium (“Random”).

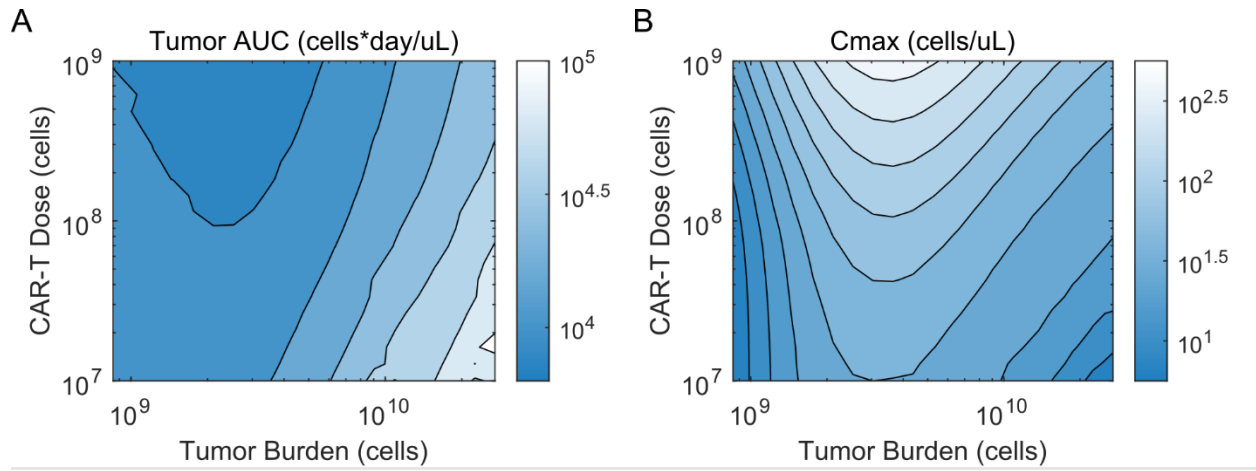


Figure S15: PKPD response depends on initial tumor burden and CAR-T dose. Model simulations were performed across a grid of CAR-T dose, initial tumor burden, and parameter set in the CR population to determine the (A) average tumor AUC and (B) average CAR-T Cmax. Tumor AUC increases with initial tumor burden and decreases with initial CAR-T dose for CR parameters. Cmax exhibits a more complex relationship, peaking for intermediate tumor burdens and generally increasing with initial CAR-T dose. This non-linear interaction between tumor burden and CAR-T dose likely contributes to the clinically observed variability.

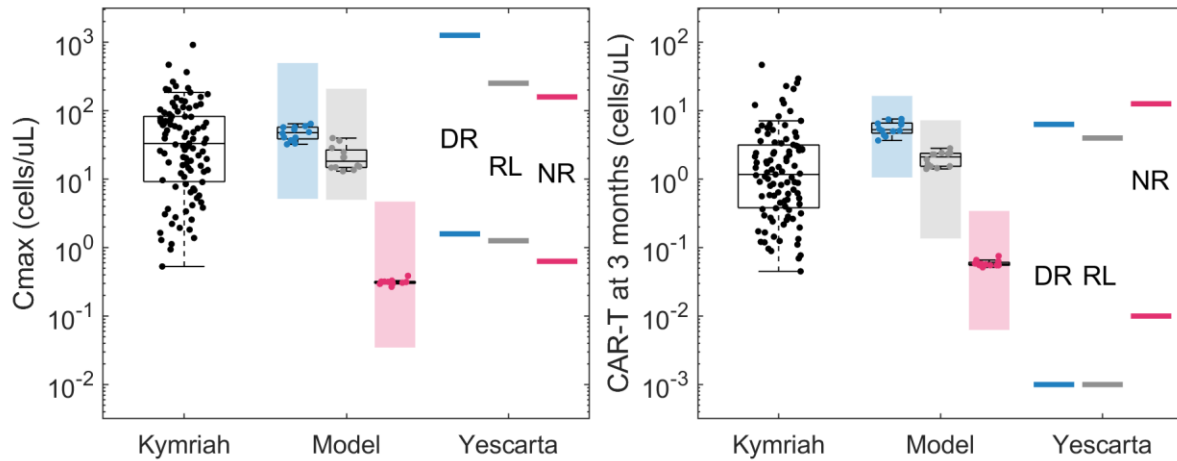


Figure S16: Comparative pharmacokinetics of Kymriah in B-ALL, our model of Kymriah in CLL, and Yescarta in LCBCL. Cmax and $C(t=3\text{ month})$ distributions for Kymriah in B-ALL and CLL were obtained via simulations of the Stein et al. model² ($n=1000$ simulations, represented as percentiles) and our model ($n=12$ simulations per group), respectively. Data for Yescarta was digitized from Locke et al.²⁴. The distributions shown for Kymriah and Model are exactly as in Figure 5C for the left panel (Cmax). The group of boxplots labelled Model show the Cmax or $C(t=3\text{ month})$ for each of the three populations (CR, blue; PR, grey; and NR, pink) with the colored background of the range of Cmax or $C(t=3\text{ month})$ obtained from the clinical PK data. Color bars for Yescarta show digitized min/max ranges of Cmax and $C(t=3\text{ month})$ while the labels (DR, durable response; RL: relapse; and NR: no response) are plotted at the approximate medians. Boxplots represent median ± 25 percentiles, and whiskers the min/max value or an additional 1.5-fold quartile distance.

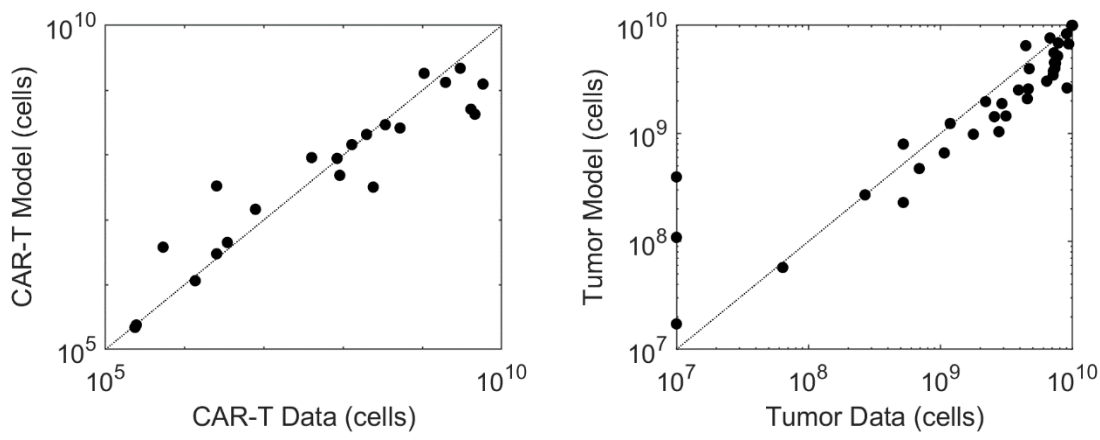


Figure S17: Goodness-of-fit plots to Abecma PKPD data. All data was fit simultaneously, with Pearson's linear correlation coefficient of 0.59 for CAR-T and 0.75 for tumors.

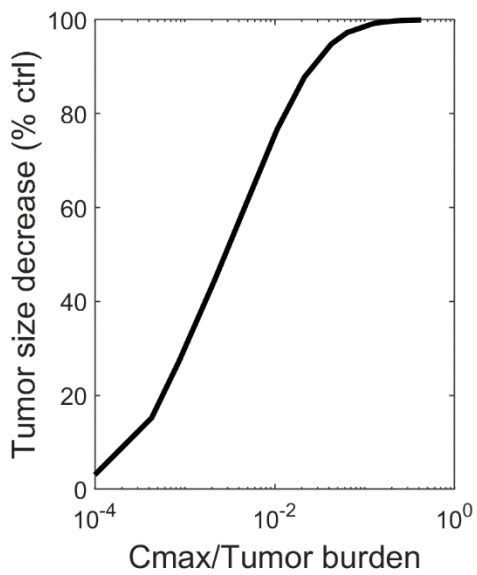


Figure S18. Cmax/Tumor burden vs. tumor response simulations for Abecma. The model fit to Abecma phase1 data was simulated at CAR-T doses ranging from 0.1 to 1000 million cells. Tumor shrinkage, compared to untreated control, was calculated at day 60. The response covariate follows the same trend as that observed for Yescarta in DLBCL and predicted for Kymriah.

REFERENCES

1. Chaudhury, A. *et al.* Chimeric Antigen Receptor T Cell Therapies: A Review of Cellular Kinetic-Pharmacodynamic Modeling Approaches. *J Clin Pharmacol* 60, S147–S159 (2020).
2. Stein, A. M. *et al.* Tisagenlecleucel Model-Based Cellular Kinetic Analysis of Chimeric Antigen Receptor-T Cells. *Cpt Pharmacometrics Syst Pharmacol* 8, 285–295 (2019).
3. Mahlbacher, G. E., Reihmer, K. & Frieboes, H. B. Mathematical Modeling of Tumor-Immune Cell Interactions. *J Theor Biol* 469, 47–60 (2019).
4. Martínez-Rubio, Á. *et al.* A Mathematical Description of the Bone Marrow Dynamics during CAR T-Cell Therapy in B-Cell Childhood Acute Lymphoblastic Leukemia. *Int J Mol Sci* 22, 6371 (2021).
5. Mueller-Schoell, A. *et al.* Early Survival Prediction Framework in CD19-Specific CAR-T Cell Immunotherapy Using a Quantitative Systems Pharmacology Model. *Cancers* 13, 2782 (2021).
6. Hardiansyah, D. & Ng, C. M. Quantitative Systems Pharmacology Model of Chimeric Antigen Receptor T-Cell Therapy. *Clin Transl Sci* 12, 343–349 (2019).
7. Mackey, M. C. Periodic hematological disorders: Quintessential examples of dynamical diseases. *Chaos Interdiscip J Nonlinear Sci* 30, 063123 (2020).
8. Singh, A. P. *et al.* Bench-to-bedside translation of chimeric antigen receptor (CAR) T cells using a multiscale systems pharmacokinetic-pharmacodynamic model: A case study with anti-BCMA CAR-T. *Cpt Pharmacometrics Syst Pharmacol* 10, 362–376 (2021).
9. Singh, A. P. *et al.* Development of a quantitative relationship between CAR-affinity, antigen abundance, tumor cell depletion and CAR-T cell expansion using a multiscale systems PK-PD model. *Mabs* 12, 1688616 (2019).
10. Kimmel, G. J., Locke, F. L. & Altrock, P. M. The roles of T cell competition and stochastic extinction events in chimeric antigen receptor T cell therapy. *Proc Royal Soc B* 288, 20210229 (2021).
11. Hirayama, A. V. *et al.* The response to lymphodepletion impacts PFS in patients with aggressive non-Hodgkin lymphoma treated with CD19 CAR T cells. *Blood* 133, 1876–1887 (2019).
12. Restifo, N. P. & Gattinoni, L. Lineage relationship of effector and memory T cells. *Curr Opin Immunol* 25, 556–563 (2013).
13. Ferreira, D. P. *et al.* Central memory CD8+ T cells derive from stem-like Tcf7 hi effector cells in the absence of cytotoxic differentiation. *Immunity* 53, 985–1000.e11 (2020).

14. Youngblood, B. *et al.* Effector CD8 T cells dedifferentiate into long-lived memory cells. *Nature* 552, 404–409 (2017).
15. Todorov, H. *et al.* CD8 memory precursor cell generation is a continuous process. *Iscience* 25, 104927 (2022).
16. Bresser, K. *et al.* Replicative history marks transcriptional and functional disparity in the CD8+ T cell memory pool. *Nat Immunol* 23, 791–801 (2022).
17. Johnnidis, J. B. *et al.* Inhibitory signaling sustains a distinct early memory CD8+ T cell precursor that is resistant to DNA damage. *Sci Immunol* 6, (2021).
18. Fraietta, J. A. *et al.* Determinants of response and resistance to CD19 chimeric antigen receptor (CAR) T cell therapy of chronic lymphocytic leukemia. *Nat Med* 24, 563–571 (2018).
19. Portet, S. A primer on model selection using the Akaike Information Criterion. *Infect Dis Model* 5, 111–128 (2020).
20. Stein, A. The cellular kinetics and anti-tumor dynamics of Kymriah. in *AcoP10* (2019).
21. Sommer, C. *et al.* Preclinical Evaluation of Allogeneic CAR T Cells Targeting BCMA for the Treatment of Multiple Myeloma. *Mol Ther* 27, 1126–1138 (2019).
22. Bai, Z. *et al.* Single-cell antigen-specific landscape of CAR T infusion product identifies determinants of CD19-positive relapse in patients with ALL. *Sci Adv* 8, (2022).
23. Haradhvala, N. J. *et al.* Distinct cellular dynamics associated with response to CAR-T therapy for refractory B cell lymphoma. *Nat Med* 1–12 (2022) doi:10.1038/s41591-022-01959-0.
24. Locke, F. L. *et al.* Tumor burden, inflammation, and product attributes determine outcomes of axicabtagene ciloleucel in large B-cell lymphoma. *Blood Adv* 4, 4898–4911 (2020).

Reporting Summary

Nature Portfolio wishes to improve the reproducibility of the work that we publish. This form provides structure for consistency and transparency in reporting. For further information on Nature Portfolio policies, see our [Editorial Policies](#) and the [Editorial Policy Checklist](#).

Statistics

For all statistical analyses, confirm that the following items are present in the figure legend, table legend, main text, or Methods section.

n/a Confirmed

- The exact sample size (n) for each experimental group/condition, given as a discrete number and unit of measurement
- A statement on whether measurements were taken from distinct samples or whether the same sample was measured repeatedly
- The statistical test(s) used AND whether they are one- or two-sided
Only common tests should be described solely by name; describe more complex techniques in the Methods section.
- A description of all covariates tested
- A description of any assumptions or corrections, such as tests of normality and adjustment for multiple comparisons
- A full description of the statistical parameters including central tendency (e.g. means) or other basic estimates (e.g. regression coefficient) AND variation (e.g. standard deviation) or associated estimates of uncertainty (e.g. confidence intervals)
- For null hypothesis testing, the test statistic (e.g. F , t , r) with confidence intervals, effect sizes, degrees of freedom and P value noted
Give P values as exact values whenever suitable.
- For Bayesian analysis, information on the choice of priors and Markov chain Monte Carlo settings
- For hierarchical and complex designs, identification of the appropriate level for tests and full reporting of outcomes
- Estimates of effect sizes (e.g. Cohen's d , Pearson's r), indicating how they were calculated

Our web collection on [statistics for biologists](#) contains articles on many of the points above.

Software and code

Policy information about [availability of computer code](#)

Data collection	Single cell RNA sequencing counts and associated metadata were retrieved from GEO (GSE197215 and GSE197268). Bulk RNA sequencing and associated metadata from Fraietta et al. (2018) was downloaded from the supplement, and all additional data was digitized from published figures using Graph Grabber v2 (Quintessa).
Data analysis	Model simulations and analysis were performed using Matlab R2021a and the SimBiology toolbox (6.1). All bioinformatics analysis was done on Ubuntu 20.04.3 LTS running R 4.1.1 (“Kick Things”). Key packages used were GSVA (1.40.1) for ssGSEA, fgsea (1.21.2) for GSEA, celldex (1.2.0) for obtaining reference datasets for SingleR (1.6.1), Seurat (4.1.0), data.table (1.14.2), limma (3.50.3), edger (3.34.1), Matrix (1.4.3) and ggplot2 (3.3.6) for data wrangling and visualization.

For manuscripts utilizing custom algorithms or software that are central to the research but not yet described in published literature, software must be made available to editors and reviewers. We strongly encourage code deposition in a community repository (e.g. GitHub). See the Nature Portfolio [guidelines for submitting code & software](#) for further information.

Data

Policy information about [availability of data](#)

All manuscripts must include a [data availability statement](#). This statement should provide the following information, where applicable:

- Accession codes, unique identifiers, or web links for publicly available datasets
- A description of any restrictions on data availability
- For clinical datasets or third party data, please ensure that the statement adheres to our [policy](#)

Provide your data availability statement here.

Human research participants

Policy information about [studies involving human research participants and Sex and Gender in Research](#).

Reporting on sex and gender

Use the terms sex (biological attribute) and gender (shaped by social and cultural circumstances) carefully in order to avoid confusing both terms. Indicate if findings apply to only one sex or gender; describe whether sex and gender were considered in study design whether sex and/or gender was determined based on self-reporting or assigned and methods used. Provide in the source data disaggregated sex and gender data where this information has been collected, and consent has been obtained for sharing of individual-level data; provide overall numbers in this Reporting Summary. Please state if this information has not been collected. Report sex- and gender-based analyses where performed, justify reasons for lack of sex- and gender-based analysis.

Population characteristics

Describe the covariate-relevant population characteristics of the human research participants (e.g. age, genotypic information, past and current diagnosis and treatment categories). If you filled out the behavioural & social sciences study design questions and have nothing to add here, write "See above."

Recruitment

Describe how participants were recruited. Outline any potential self-selection bias or other biases that may be present and how these are likely to impact results.

Ethics oversight

Identify the organization(s) that approved the study protocol.

Note that full information on the approval of the study protocol must also be provided in the manuscript.

Field-specific reporting

Please select the one below that is the best fit for your research. If you are not sure, read the appropriate sections before making your selection.

Life sciences Behavioural & social sciences Ecological, evolutionary & environmental sciences

For a reference copy of the document with all sections, see nature.com/documents/nr-reporting-summary-flat.pdf

Life sciences study design

All studies must disclose on these points even when the disclosure is negative.

Sample size

all data used in this study was digitized from publications or downloaded, hence we had no control over clinical/experimental replicates. For stochastic algorithms (i.e. virtual population numbers, model fitting runs), sample sizes were chosen heuristically. That is, algorithms were run repeatedly at different depths to assess the stability of results. Iteration depths were then selected as those that generated consistent results while minimizing compute time. e.g. n=12 PSO runs at 100 particles x 100 iterations per-population, n=1000 virtual subjects per simulation, n=2500 classifier train/test split iterations.

Data exclusions

no data was excluded

Replication

computational replication was performed as described above to assess the stability of stochastic algorithms.

Randomization

computational randomization was performed where applicable to assess model predictions against null distributions. Parameter space scans to assess model goodness-of-fit, and random classification to assess predictive accuracy of the transcriptome classifier.

Blinding

Its not possible to perform computational analyses blinded.

Reporting for specific materials, systems and methods

We require information from authors about some types of materials, experimental systems and methods used in many studies. Here, indicate whether each material, system or method listed is relevant to your study. If you are not sure if a list item applies to your research, read the appropriate section before selecting a response.

Materials & experimental systems

- | | |
|-------------------------------------|-------------------------------|
| n/a | Involved in the study |
| <input checked="" type="checkbox"/> | Antibodies |
| <input checked="" type="checkbox"/> | Eukaryotic cell lines |
| <input checked="" type="checkbox"/> | Palaeontology and archaeology |
| <input checked="" type="checkbox"/> | Animals and other organisms |
| <input checked="" type="checkbox"/> | Clinical data |
| <input checked="" type="checkbox"/> | Dual use research of concern |

Methods

- | | |
|-------------------------------------|------------------------|
| n/a | Involved in the study |
| <input checked="" type="checkbox"/> | ChIP-seq |
| <input checked="" type="checkbox"/> | Flow cytometry |
| <input checked="" type="checkbox"/> | MRI-based neuroimaging |